Volume 5
Number 1
January 2026
Pages 1–132

Energy Advances

rsc.li/energy-advances

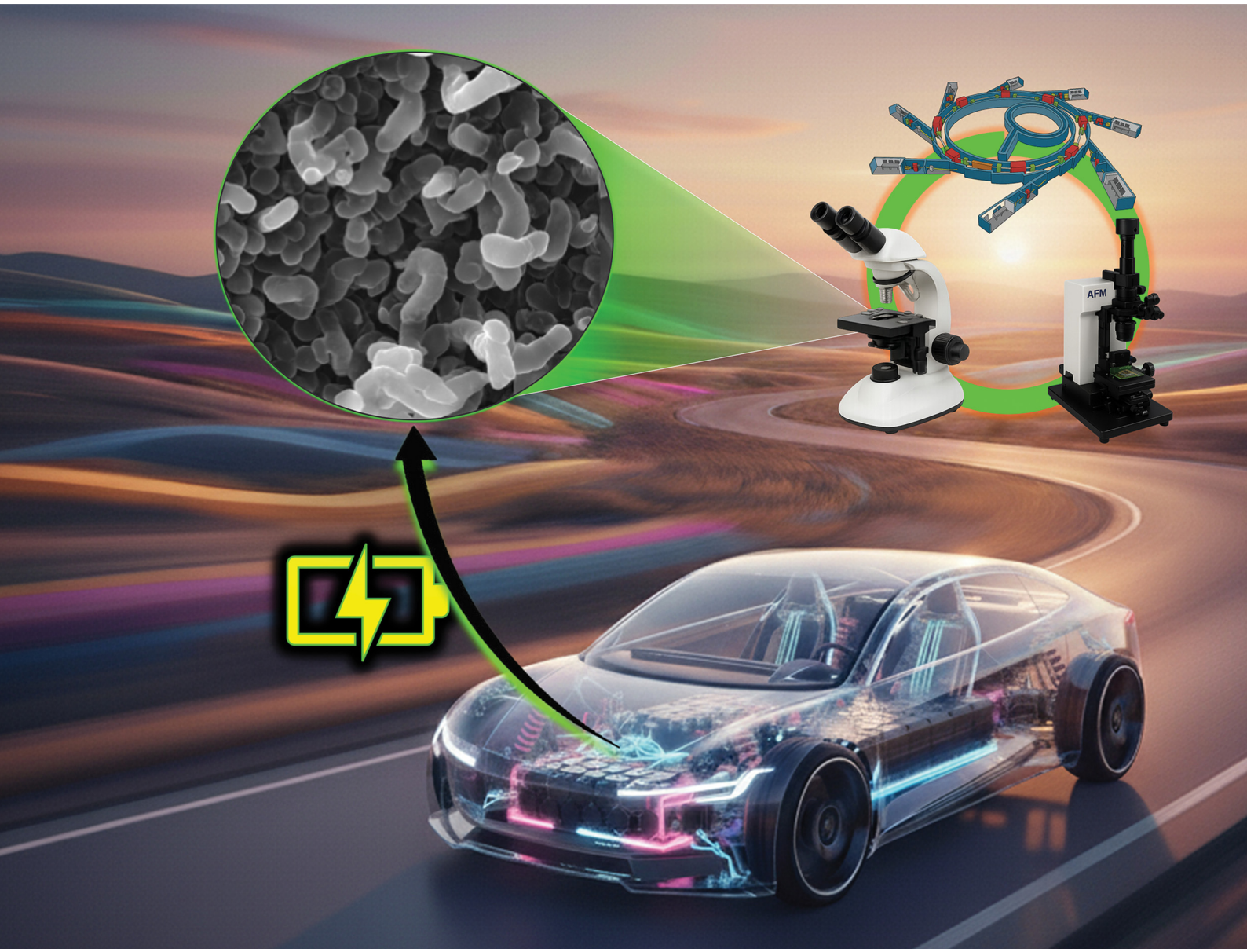

ISSN 2753-1457

ROYAL SOCIETY OF CHEMISTRY

REVIEW ARTICLE
Xiangbo Meng *et al.*
In situ and *operando* microscopy studies on lithium metal anodes: a review

Energy Advances

ROYAL SOCIETY OF CHEMISTRY

REVIEW ARTICLE

View Article Online
View Journal | View Issue

Cite this: *Energy Adv.*, 2026, **5**, 7

In situ and *operando* microscopy studies on lithium metal anodes: a review

Ian Lindsey,†[a] Cameron Mondl†[b] and Xiangbo Meng *[ab]

Lithium metal is regarded as an ultimate anode for rechargeable batteries, ascribed to its extremely high capacity. Its implementation can remarkably boost the energy density of the resultant lithium metal batteries. However, it is very challenging to commercialize lithium metal anodes, primarily due to the intertwined nature of the formation of a solid electrolyte interphase (SEI) and the growth of lithium dendrites. To understand these issues and therefore develop technical solutions, various instrumental techniques have been employed. This review highlights the most recent advancements of *in situ* and *operando* microscopy studies that are critical for investigating and addressing the issues related to SEI and lithium dendrites, including optical, electron, and atomic force microscopies. Low magnification *in situ* optical microscopy techniques are used to analyze dendrite morphology behaviors, the development of capping layers after cycling, and the impact of various dendrite suppression methods. High magnification *in situ* scanning electron microscopy enables more detailed dendrites and interface evolution analysis, revealing complex behavior mechanisms over extended cycling. While *in situ* transmission electron microscopy techniques can also investigate dendrite nucleation and morphology, they are particularly valuable in characterizing the SEI layer development at unparalleled spatial resolution. Additionally, *in situ* atomic force microscopy contributes valuable information for identifying the SEI layer growth through surface topology and force mapping. Together, these microscopy studies help us advance a better understanding on the underlying mechanisms of the formation of the SEI and lithium dendrites. They also are valuable for us to develop solutions for commercializing lithium metal anodes for high-energy lithium metal batteries.

Received 21st August 2025,
Accepted 30th October 2025

DOI: 10.1039/d5ya00240k

rsc.li/energy-advances

1. Introduction

The first report on lithium (Li) metal anodes (LMAs) was documented in 1976 by Stanley S. Whittingham.[1] Li metal is considered an ideal anode material for next-generation rechargeable batteries because of its very low electrochemical

[a] *Department of Mechanical Engineering, University of Arkansas, Fayetteville, AR 72701, USA. E-mail: xbmeng@uark.edu*
[b] *Materials Science & Engineering, University of Arkansas, Fayetteville, AR 72701, USA*
† The authors contributed equally.

Ian Lindsey

Mr Ian Lindsey was a Master's student of mechanical engineering at the University of Arkansas (Fayetteville, AR), USA, working as a research assistant under the supervision of Dr Xiangbo (Henry) Meng (May 2024–July 2025). He earned his Bachelor's degree from the same department in 2024. His research focused on lithium metal batteries and electrode/electrolyte interfaces for energy storage devices.

Cameron Mondl

Mr Cameron Mondl is a Master's student of materials science at the University of Arkansas, USA, working as a research assistant under the supervision of Dr Xiangbo (Henry) Meng (2024 – present). He earned his Bachelor's degree from the University of Missouri (Columbia, MO), USA, in 2023. His research focuses on lithium metal batteries and electrode/electrolyte interfaces for energy storage devices.

potential (−3.04 V *vs.* the standard hydrogen electrode (SHE)), low density (0.59 g cm^{-3}), and high specific capacity (3860 mAh g^{-1}).[2] Although Li metal has the most desirable attributes of a premium anode material, it suffers from two main issues: continuous formation of the so-called solid electrolyte interphase (SEI) and dendritic growth (or dendrites) during plating. These two issues pose big challenges in performance and safety for commercializing LMAs in Li metal batteries (LMBs). As a consequence, lithium-ion batteries (LIBs) were developed in the 1980s and commercialized in the 1990s, in which graphite and $LiCoO_2$ were adopted as the anode and the cathode, respectively.[3–5] However, graphite anodes have a moderate capacity, ∼372 mAh g^{-1}, which significantly limits the energy density of LIBs, <250 kWh kg^{-1}. In pursuing a fully electrified society, rechargeable batteries enabling an energy density of >300 kWh kg^{-1} are urgently needed by electric vehicles (EVs). To this end, LMBs are very promising for achieving an energy density of >400 kWh kg^{-1}. Consequently, LMAs have been revived and are undergoing intensive investigations.

Rechargeable Li-based batteries, including LIBs and LMBs, operate by transporting Li^+ ions through a liquid electrolyte and electrons through an external circuit between their anode and cathode during charge and discharge. The electrolyte can exist stably between the two electrodes in an electrochemical stability window (ESW). The ESW of an electrolyte is represented by the energy levels of the highest occupied molecular orbital (HOMO) and the lowest unoccupied molecular orbital (LUMO) of its solvent molecules.[6] The ESW of an electrolyte is always lower than its HOMO–LUMO energy gap based on the Fermi level concept.[7] Because Li metal has such a low electrochemical potential, the commonly used electrolytes are usually not stable upon contacting a Li surface. The reaction between an electrolyte and Li produces an interface layer, *i.e.*, the so-called SEI. An SEI layer would be ionically conductive, allowing Li^+ ions to diffuse uniformly to the Li metal surface, and electronically resistant, preventing electrons from reaching the electrolyte furthering the reduction and thickening of the SEI. Other positive attributes of the SEI would be uniformity of thickness and ionic conductivity, and mechanical robustness to prevent cracking due to stress from electrode volume change. Because of the mosaic nature of the SEI that is formed without interfacial engineering efforts, however, the ionic conductivity and thickness of the SEI layer both vary across the surface.[8] The result of a nonuniform SEI is that Li^+ ions will preferentially plate in certain locations (hot spots) at higher current than other areas, as described by Sanchez *et al.*[9] This preferential plating will compound with the nucleation of dendrites at that original hotspot. As the dendrite grows, it effectively casts a shadow in the electric field, increasing the preferential plating of Li^+ ions onto that dendrite.[10] As dendrites grow, they push against or break through the existing SEI layer, exposing Li metal to fresh electrolyte, causing more electrolyte to decompose, reducing the active material inside the electrolyte, and eventually, after many cycles, drying the battery and prematurely ending the life of the battery. Before this point, the consumption of the electrolyte is ever reducing the coulombic efficiency (CE) of the battery.

Dendrites have their own host of harmful effects on battery life and performance. Because of the morphology of dendrites, they are easily broken from the surface, either mechanically or electrically, making those detached dendrites dead lithium, and preventing them from contributing to electrochemical reactions in the future. Dead Li reduces the active material in the battery and greatly reduces the CE of the battery and can eventually consume all of the active Li in the battery, ending its life.[11] Lastly, dendrites can penetrate the separator and thereby short the battery. These shorts can lead to thermal runaway and eventually ignite the very flammable electrolyte, leading to dangerous fires or combustion.

It is for these reasons that both the SEI and dendrite propagation on Li metal and other electrodes must be investigated in a tandem fashion. This is where *in situ* and *operando* studies are paramount. *In situ*/*operando* optical microscopy (OM) studies are generally focused on visualizing the evolutions of dendritic morphologies in a real-time mode. However, OMs are limited in their resolutions, typically at the micron level. Compared to OMs, *in situ* scanning electron microscopy (SEM) can visualize the morphological evolutions of Li dendrites and SEI formation at much higher resolutions at the nanoscale.[12] Similar to SEM, *in situ* transmission electron microscopy (TEM) also can track morphological evolutions of Li dendrites and SEI layers at the nanoscale with a time-resolved mode. They can also provide information about materials composition and crystallinity, which is important for analyzing the SEI and Li dendrites. Atomic force microscopy (AFM) mainly provides surface information about the electrode surface at the nanoscale, even under non-vacuum or liquid conditions.[13] More

Xiangbo Meng

Dr Xiangbo (Henry) Meng is an associate professor of mechanical engineering at the University of Arkansas (Fayetteville, AR). He has two PhD degrees: one in mechanical & materials engineering (2011) and another in chemical & biochemical engineering (2008), both from the University of Western Ontario (London, ON), Canada. He carried out his postdoctoral research at Argonne (Lemont, IL) and Brookhaven (Upton, NY) National Laboratories, USA, from 2011 to 2016. Since he joined the University of Arkansas in 2016, he has been directing a research group conducting studies in three main areas: (1) highly tunable synthesis of nanoscale materials using atomic and molecular layer deposition (ALD and MLD); (2) accurate interface engineering of advanced batteries via ALD and MLD, including lithium-ion batteries, lithium metal batteries, sodium-ion batteries, sodium metal batteries, and solid-state batteries; and (3) precise surface engineering for improved properties (such as wear and corrosion resistance) using ALD and MLD.

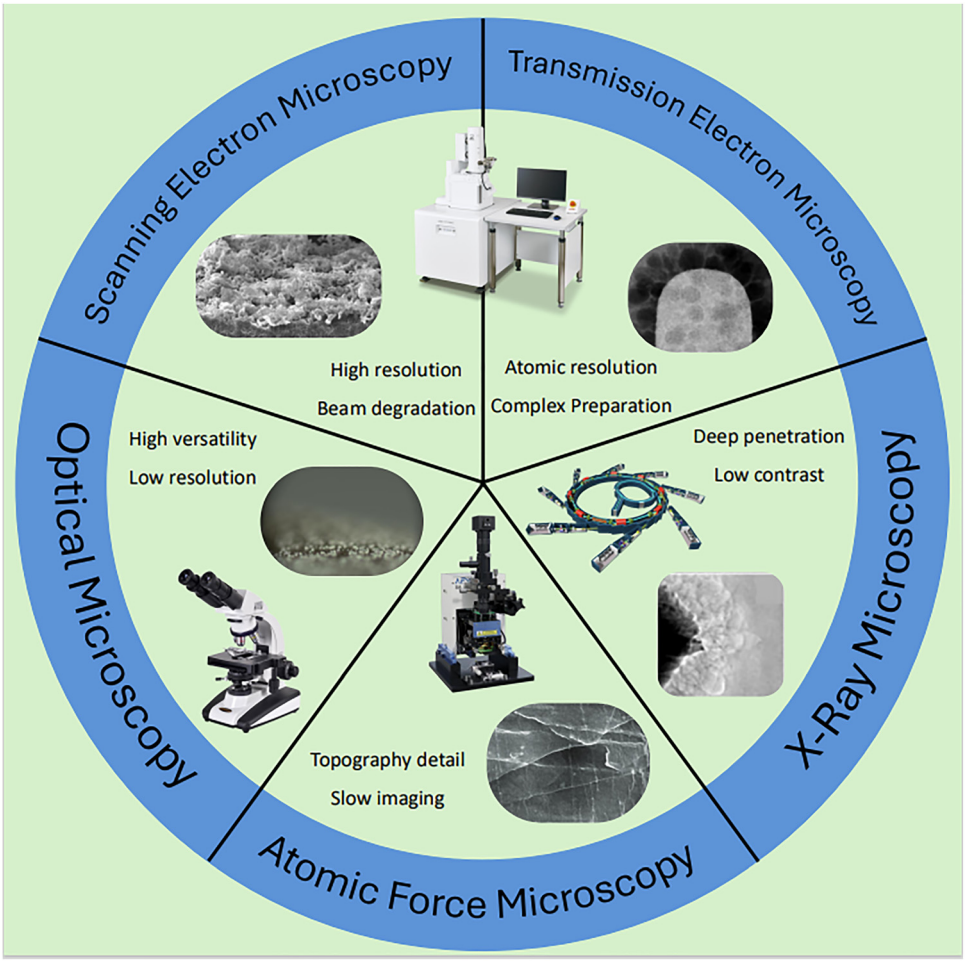

Fig. 1 A schematic illustration for comparatively describing the different microscopic techniques of LMAs, including optical microscopy, atomic force microscopy, scanning electron microscopy, transmission electron microscopy, and synchrotron-based X-ray microscopy.

recently, X-ray microscopic techniques have been explored and utilized for studying LMAs, which use X-rays to visualize the dynamic processes of Li-plating and stripping at high resolution. All these five microscopic instruments/facilities are complementary in their capabilities, as illustrated in Fig. 1. The combination of these techniques provides a broad wealth of information that has advanced the understanding of Li dendrite and SEI behavior during battery cycling. This review examines the results of research studies utilizing these *in situ* microscopy techniques and explores fundamental conclusions of Li metal anodes.

Following this introduction, we focus on summarizing the latest efforts using *in situ* OM, SEM, TEM, and AFM for studying the issues of LMAs. Finally, we conclude our literature investigation with an outlook on future studies.

2. *In situ* optical microscopy studies on Li dendrites

LMAs can be used with liquid electrolytes and solid electrolytes. Consequently, they have been studied in liquid cells and solid cells.

2.1. Li stripping/plating behaviors in liquid cells

One of the most effective ways to study LMAs is to use symmetrical cells. Symmetrical cells remove the various factors contributed by cathodes, as a choice of which can vary the performance of the LMA, effectively skewing results around the Li electrode. Symmetrical cells consist of a working and a counter electrode, both of which are comprised of a Li metal chip or Li metal deposited onto a substrate (*e.g.*, Cu foil). Reference electrodes may also be used to decipher what is happening at either side of the cell during an electrochemical experiment, as will be discussed later. During symmetrical cell testing, a current is passed through the cell *via* a potentiostat or galvanostat. When a negative current is passed through the cell, electrons are pulled from the counter electrode and are gathered on the working electrode. Li^+ ions are stripped from the counter electrode and transported into the concentration of the electrolyte. At the other end of the cell, Li^+ ions from the concentration in the electrolyte are plated onto the working electrode where they meet with electrons supplied by the external circuit. During this process, Li dissolution (or Li stripping) forms pits on the surface of the counter electrode and Li deposition (or Li plating) forms dendrites on the surface

of the working electrode. As previously discussed, this is where optical microscopy becomes a valuable tool in evaluating LMAs.

An *in situ* OM when paired with the overpotential profiles during galvanostatic plating and stripping half-cycles can help visualize the processes happening on the surface of the Li metal electrodes and thereby help identify which processes contribute and how much they contribute to the impedance across the cell. Wood *et al.* conducted an early study on LMAs using symmetrical cells *via* OM and synchronized electrochemical data.[14] They developed a custom visualization cell, and through *operando* observations during galvanostatic cycling, elucidated a correlation between the behavior of the voltage profile and what was visually recorded on the surface of the Li metal working electrode. They made the first set of observations using 1 M Li hexafluorophosphate ($LiPF_6$) in 1 : 1 ethylene carbonate/dimethyl carbonate (EC : DMC) electrolyte, *i.e.*, 1 M $LiPF_6$ in 1 : 1 EC : DMC. The current density applied in both the stripping and plating step was 5 mA cm^{-2}, while both the working and counter electrodes were Li metal chips. A pristine Li metal surface could be seen before the first half-cycle without any current applied (Fig. 2(a)). During the first half-cycle, the overpotential starts at a peak near 0.6 V with a quick, then slower decline toward the zero volt (Fig. 2(b)). Dendrites nucleate and grow larger during this half-cycle with more growth out of focus in the background. In the second half-cycle, a local minimum peak of voltage gives way to a plateau closer to zero (Fig. 2(c)). During this initial peak and plateau of the second half-cycle, dendrites shrink, then the color of the dendrites darkens to black as the voltage grows to a second peak (Fig. 2(d)). At the climax of this second peak, the dendrites stop getting darker and stop shrinking, and pits can be seen beginning to nucleate, as seen in the yellow circles of Fig. 2(e). As these pits deepen, the voltage trends toward zero again. In the third and final half-cycle of this analysis, a similar overpotential profile of the last half-cycle is observed along with new dendrite nucleation and growth in the pits previously formed (Fig. 2(f)).

Using these observations as well as the Nernst–Planck equation in one dimension, they developed a numerical model to further explain the electrochemical behavior in Li metal symmetrical cells. Their findings showed that once a dendrite has nucleated, the kinetics of the surface area of the dendrite is much faster than the kinetics of the bulk Li metal. Thus, during the first half-cycle, deposition kinetics improves as dendrites nucleate and grow larger, leading to a decrease in cell voltage from an initial maximum. When cell polarity is switched, the kinetics of plating onto the counter electrode are slow while the stripping from old dendrites is fast. Dendrites grow on the surface of the counter electrode, decreasing the voltage until another peak begins to form. This second peak forms because the dendrites on the working electrode are no longer able to supply Li^+ ions to the electrolyte because they have become mechanically or electrically detached from the electrode and can no longer participate in the electrochemical operations. This is called dead Li and is evidenced by the black color of the dendrites seen in Fig. 2(d). This causes the ratio of the area with fast kinetics to the area with slow kinetics to become small, forcing stripping to occur from the bulk Li – causing a second peak, and pits to form (Fig. 2(e), yellow circles). To further explain these conclusions, they conducted a similar experiment with a three-electrode cell. The contributions of the anode and cathode during each half-cycle expose the reasons behind the peaks and plateaus of the overpotential profile. In the first half-cycle, the shape of the cathode, where deposition occurs dictates the shape of the overpotential of the cell (Fig. 2(g)). This is because the growth of dendrites, and higher surface area drastically increases the kinetics of deposition. Next, the counter electrode is plated onto, and its potential change produces the first peak, while the switching from stripping of dendrite to stripping of bulk Li produces the second peak contributed by the anode. A similar trend is shown in the following cycles. By observing the surface of both electrodes and the overpotential curve during galvanostatic cycling in real time, the group was able to elucidate the fundamental mechanisms of Li symmetrical cells.

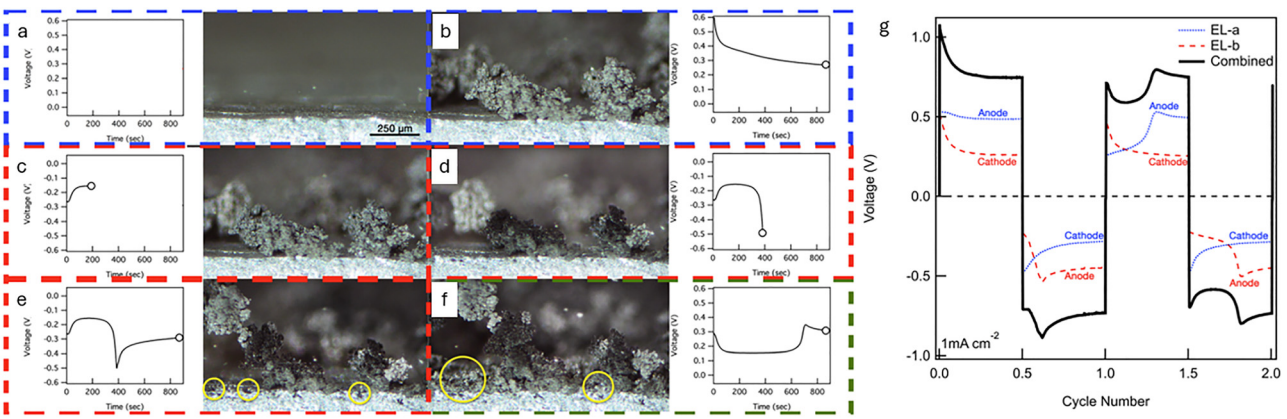

Fig. 2 *Operando* OM observations matched with the overpotential profiles of the cell. Initial surface (a), first plating half-cycle (b), second plating half-cycle (c)–(e), and third stripping half-cycle (f). (g) Voltage profile of the Li symmetrical cell with reference electrode readings splitting the contributions of the anode and the cathode in the first 2 cycles. Reprinted (adapted) with permission from ref. 14 under a Creative Commons Attribution (CC BY) license.

The same team conducted a subsequent study using an OM cell with a planar viewpoint instead of a cross-section view as the previous study did. Sanchez *et al.* modified an OM visualization cell to optimize the current density across the working electrode surface and observe dendrite and pit nucleation and morphology during galvanostatic plating.[9] Their initial observations confirmed those made previously by Wood *et al.* with a new point of view. To expand on these findings, they observed dendrite and pit nucleation at varying current densities. They conducted experiments using 1 M $LiPF_6$ in 1 : 1 by volume EC : EMC (ethyl methyl carbonate) electrolyte. They observed an increase in the number of nucleation sites for dendrites and for pits as the current density increased (Fig. 3(a)–(f)). Although many factors (*e.g.*, electrolyte, cell geometry, surface preparation, *etc.*) affect nucleation density, the positive correlation reveals the undeniable role of surface heterogeneity in Li dissolution and deposition. The activation barrier for nucleation varies across the surface due to surface defects, SEI composition and thickness, topographical features and more. At low current densities, the activation barrier for nucleation is reached only at areas across the surface with a low activation barrier. At high current densities, the areas with a low activation barrier as well as the areas with high activation barrier for nucleation are reached leading to more nucleation sites. They further revealed the role of surface defects and grain boundaries. As shown in Fig. 3(g)–(j), grain boundaries create areas of low activation barriers for nucleation, leading to preferential plating at those points.

Using their modified planar view OM visualization cell, the team also observed the impact of dendrite size on the formation of dead Li. The group developed a scheme for estimating the effective volume of each dendrite observed from above, where an effective radius is estimated from the projected area as viewed from above, and an effective dendrite volume is calculated (Fig. 3(k)). Four dendrites were measured and observed as they increased in volume over a deposition and dissolution cycle at a current density of 3 mA cm^{-2}. During deposition, all dendrites grow in volume at different rates to a maximum at which polarity is switched. When dissolution begins, the dendrites shrink, some for longer than others. By approximately half-way through the dissolution step, however, all dendrites had stopped shrinking. Because the cell was still undergoing dissolution and the dendrites were staying the same size, the group concludes that these dendrites had become mechanically or electrically isolated from the bulk Li and were no longer participating in the electrochemical reactions. In other words, they had become dead Li. More of these studies at varying current densities were carried out and their results are quantified by comparing the results across varying capacities. By plotting the dead Li effective volume *versus* the maximum effective volume for the first two cycles in a Li symmetrical cell, a linear relationship between the two was observed for both cycles in all current densities. A steeper slope implies that a larger maximum effective volume can be reached while more of that dendrite will be stripped away before becoming detached and being measured as dead Li. The steeper slope of the second cycle implies that the second cycle yields more reversible deposition than the first cycle. This observation is confirmed by the comparison of the overpotential curves. As previously discussed, the second peak of an

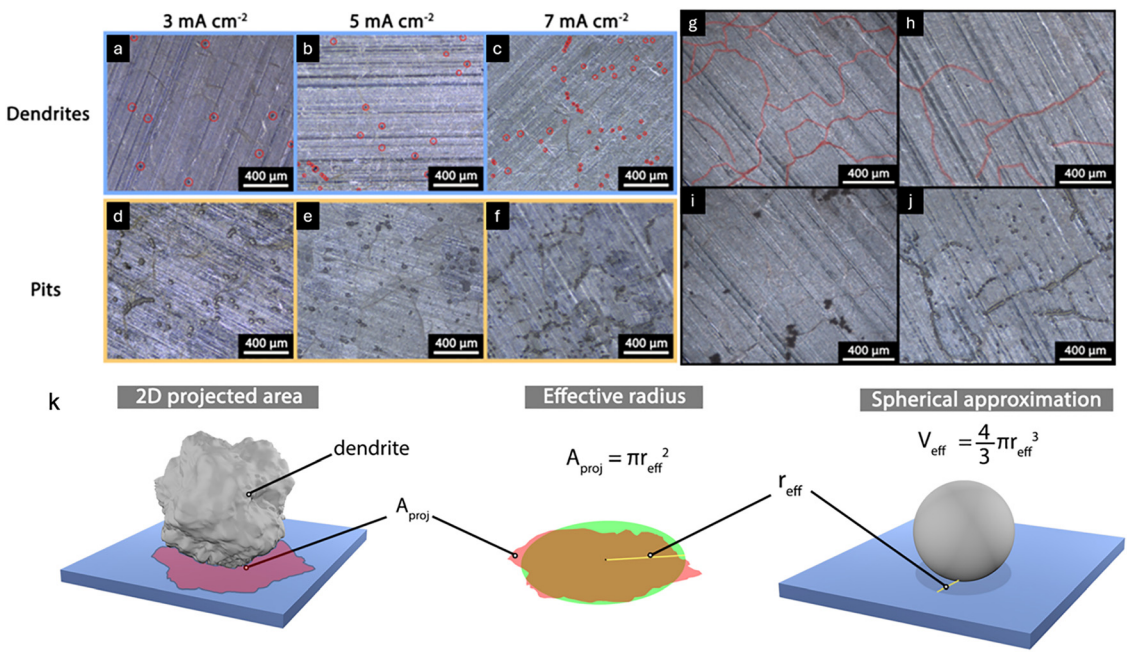

Fig. 3 (a)–(c) Dendrite nucleation highlighted in red after 0.0025 mAh cm^{-2} at 3, 5, and 7 mA cm^{-2} respectively. (d)–(f) Pit nucleation after 0.2 mAh cm^{-2} at 3, 5, and 7 mA cm^{-2} respectively. (g) and (h) Pristine Li surface with grain boundaries highlighted in red. (i) Same surface as panel g after 0.01 mAh cm^{-2} of Li deposition. (j) Same surface as panel h after 0.2 mAh cm^{-2} of Li dissolution. (k) Dendrite area estimation method from the measured top-view radius. Reprinted (adapted) with permission from ref. 9. Copyright (2020) American Chemical Society.

overpotential curve of a Li symmetrical cell is caused by the switching of dissolution occurring from dendrites to dissolution occurring from the bulk Li.[14] If this peak occurs later in the half-cycle, more stripping is occurring from the dendrites before dead Li is formed. Both the OM observations of dead Li effective volume and the second peak observations of the overpotential curves provide solid evidence that the second cycle of a Li symmetrical cell leads to more reversible Li deposition. These observations using a modified OM visualization cell led researchers to the fact that the nucleation of dendrites in previously formed pits is the most reversible nucleation site possible without the addition of surface engineering to improve LMA reversibility.

One of the earliest OM investigations of Li metal deposition was made by Steiger *et al.*[15] They observed deposition onto a tungsten substrate working electrode with Li supplied by a reservoir of Li metal attached to a tungsten counter electrode. They utilized 1 M $LiPF_6$ in 1 : 1 by weight EC : EMC electrolyte and a novel visualization cell with a poly-ethylene frame and a borosilicate glass window. As shown in Fig. 4(a)–(d), they observed a base growth for a dendrite under a deposition current of 2 μA cm^{-2}. Because the original body did not change shape as it was pushed along by its growth, they designate this as a base growth. They also observed growth at the tip of a dendrite. Fig. 4(e) and (f) show a kink formed while Fig. 4(g) and (h) show a dendrite extrude from the kink, indicating growth at the tip of the dendrite. Additionally, Fig. 4(i)–(k) depict the most obvious of the observations: a dendrite formation resembling a loop extends in width as deposition continues. Based on *ex situ* SEM observations, they clarified that the tip growth occurs behind a small inactive structure at the tip. Based on these OM observations, they concluded that Li insertion primarily occurs at crystalline defects in the dendrites. This is well in agreement with the observations previously mentioned regarding insertion at defects in the bulk Li surface.

Differently, Bai *et al.* utilized a novel capillary cell to exploit the difference between reaction-limited and transport-limited growth modes of Li dendrites.[16] They conducted a plating half-cycle through the specialized visualization cell and observed the deposition onto the Li metal electrode for up to 3000 s. As Li deposits, the concentration gradient from the electrode surface into the electrolyte gets steeper and less ions are available for diffusion onto the surface of the dendrites. After a certain time, or capacity, namely Sand's Capacity, the deposition mechanism switches from being limited by the kinetics of the reaction to being limited by the transport of Li ions through the electrolyte near the surface of deposition. At this point, dendrites switch from having a mossy morphology, to a whisker morphology, which is easily visible through the optical observations made. Through *ex situ* SEM, they showed that this growth mode is responsible for premature cell shortage *via*

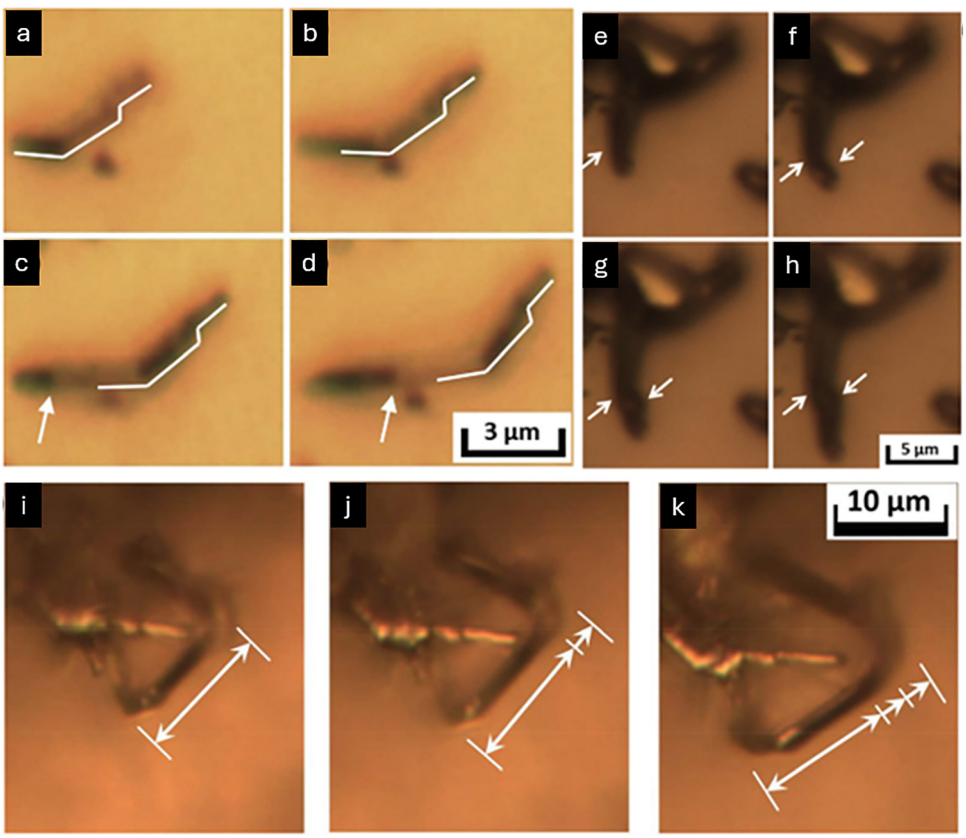

Fig. 4 (a)–(d) Observation of base growth of Li dendrite. (e)–(h) Observation of tip growth of Li dendrite. (i)–(k) Observation of dendrite growth between kinks. Reprinted (adapted) with permission from ref. 15. Copyright (2014) Elsevier.

dendrite penetration through porous separators. OM visualization allowed them to visually identify when Sand's capacity had been reached and when dangerous deposition of Li was taking place.

Using OM and phase field simulations, Shen *et al.* generated a different perspective on the formation of aggregated Li dendrites.[10] They conducted plating half-cycles at 0.5 and 3.0 mA cm^{-2}, respectively. Vast differences in dendrite morphology between 3.0 and 0.5 mA cm^{-2} were observed during their *in situ* OM observations. They further showed the difference in morphology using *ex situ* SEM. They proposed that the Li morphology is not a product of different reaction-limiting aspects, but rather a difference in electric field surrounding the deposition sites. Deposition begins in certain areas before others along the surface of the electrode,[14] resulting in fluctuations of electric field across the surface, making deposition more accessible to Li^+ ions for areas that nucleated first. As these dendrites grow, they cast a shadow around the dendrites that nucleated around them, not allowing further Li insertion to occur. They then conducted electric field distribution simulations at the two current densities described. These electric field distributions reveal a shadow effect that prevents uniform Li^+ ion diffusion except onto the already towering dendrites that propagated due to the process described by Sanchez *et al.*[9] This proposed model for morphology variations is in good agreement with observations made by the other groups depicting preferential plating onto surface defects[9] and previously formed dendrites.[14]

Of various efforts, one study deserving a special discussion is the recent work by Huang *et al.*[17] They developed an *operando* OM technique enabling quantitative monitoring of the evolution of Li growth layer and capping layer thickness and porosity upon the Li plating/stripping processes. In their study, 5 different electrolytes were adopted: 1 M $LiPF_6$ in 1 : 1 by volume EC : DEC (diethyl carbonate) alone (named as the baseline electrolyte), with 1 wt% cesium hexafluorophosphate ($CsPF_6$), with 1 wt% lithium difluoro(oxalate)borate (LiDFOB), with 5 wt% fluoroethylene carbonate (FEC), and with 1 wt% lithium difluorophosphate (LPF) as additives to the baseline electrolyte. They studied the Li deposition in the Li‖Cu cell configuration, as illustrated in Fig. 5(a). The received images could be further processed to quantify the morphology, thickness, and porosity of the deposited Li. As illustrated in Fig. 5(b), for example, the Li‖Cu cell was cycled under different current densities while the OM could visualize the morphological evolution of Li deposition with time, using the electrolyte 1 M $LiPF_6$ in 1 : 1 EC/DEC with 1 wt% $CsPF_6$. The as-received information is very insightful for understanding the Li plating/stripping behaviors in the electrolyte. Similarly, the team conducted *operando* OM investigations with the other electrolytes. Through quantitative analysis on the OM results, they concluded that FEC- and LPF-based electrolytes are favorable for suppressing Li dendrites. Based on their OM results, furthermore, they categorized the Li plating/stripping behaviors in these electrolytes into three types. The first is the filament type (Fig. 5(c)) and the LiDFOB-added electrolyte contributed to this, due to the poor robustness of the as-formed SEI. The second is the moss-like type (Fig. 5(d)) and the $CsPF_6$-added electrolyte led to this, ascribed to the higher robustness of the as-formed SEI. The third is the ideal columnar type (Fig. 5(e)), while FEC- and LPF-based electrolytes are favorable for this type, due to the robust as-formed SEI.

Chen *et al.* also investigated the build-up of dead Li and its effect on the overpotential profile after extended cycling in symmetrical Li metal cells.[18] They observed a change in overpotential curves from the peaking behavior to an arc and plateau at extended cycles in concordance with a buildup of dead Li observed *via* OM. The group proposed the change in overpotential shape and increase in total was due to the tortuous pathway of diffusion through the layer of dead Li accumulated at many cycles. Li ions cannot diffuse through the layer as fast as they can through pristine liquid electrolyte, therefore after many cycles, the concentration gradient through the layer becomes steep. Their hypothesis was evidenced by OM observations of the buildup of this layer, and they proved the validity of this hypothesis using a galvanostatic intermittent titration technique (GITT). GITT is a cycling technique that allows time for the ionic concentration near the surface of the electrode to normalize, thus removing the effect of mass transport in the voltage profile. During GITT, current is applied for 15 s then a 3 min rest follows, this is repeated until 0.25 mAh cm^{-2} is plated or stripped. The rest periods are then removed from the graph depicting the overpotential profiles for clearer interpretation. At low cycles the GITT overpotential profiles were the same as galvanostatic cycles, however at high cycles the GITT overpotential profiles exhibited the same peaking and plateaus while the galvanostatic cycling profiles had changed into an arc shape with increased overpotential maximums.

Overall, *in situ* OM studies using liquid cells reveal how Li dendrite growth initiates at surface defects and grain boundaries, with higher current densities increasing both dendrite and pit nucleation. Dendrites grow preferentially in pre-existing pits and can become dead Li when mechanically or electrically isolated, evidenced by OM-observed volume retention during dissolution and corresponding overpotential peaks. Modified OM cells enabled quantification of dendrite volume, capping layer porosity, and growth reversibility, showing that FEC and LPF additives produce denser, more stable Li deposits.

2.2 Li stripping and plating in solid cells

In addition to the studies discussed above using liquid electrolytes, OM is also a valuable tool in analyzing Li plating through solid electrolytes. Porz *et al.* observed Li deposition through 4 inorganic solid electrolytes with OM,[19] including amorphous 70 : 30 mol% $Li_2S : P_2S_5$ (glassy LPS), polycrystalline β-Li_3PS_4, and polycrystalline and single-crystalline $Li_6La_3ZrTaO_{12}$ garnet (LLZTO). A point electrode was pressed onto two locations of the glassy LPS electrolyte, one location was free of any visible surface defects, and the other location was scratched with a diamond-tipped tool. Li metal was deposited through the electrolyte onto the point electrode for 20 h at 0.8 μA (10 mA cm^{-2} based on point electrode surface area). At the

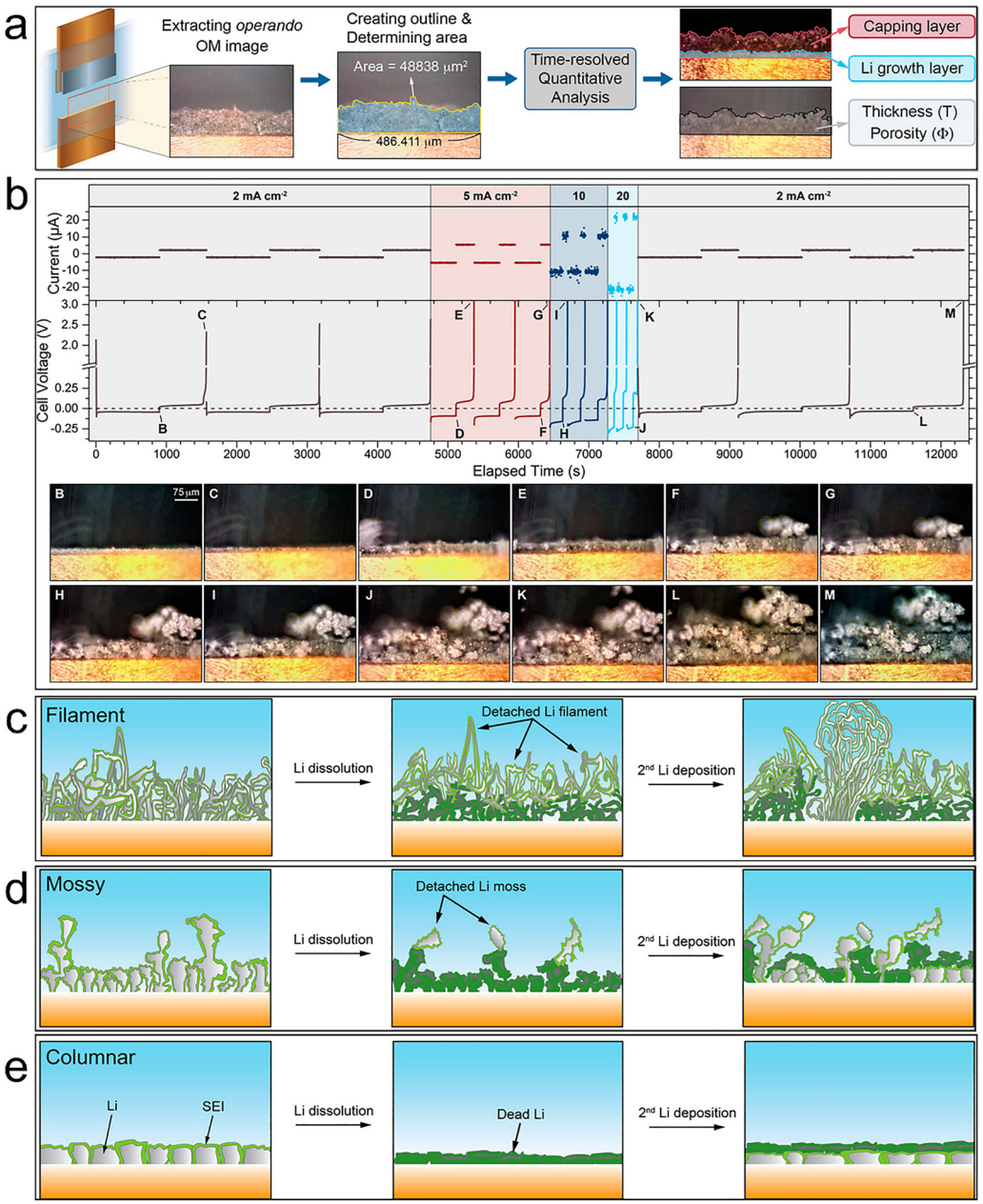

Fig. 5 An *operando* optical microscopy technique enabling quantitative analysis of OM results. (a) The *operando* OM system. (b) The *operando* study on Li plating/striping using the electrolyte 1 M $LiPF_6$ in 1 : 1 EC/DEC with 1 wt% $CsPF_6$ at varying current densities (2–20 mA cm^{-2}). Schematic illustrations of Li plating/stripping behaviors in different electrolytes: (c) Li filament, (d) mossy Li, and (e) the ideal Li in columnar structures. Reprinted (adapted) with permission from ref. 17. Copyright (2023) American Chemical Society.

location without defects, Li metal plated onto the surface of the electrode without observation of cracking. On the surface with defects, however, crack propagation and growth were observed *via* OM and no deposition was observed on the electrode. The results are illustrated in Fig. 6(a)–(h), along with the experimental setup in Fig. 6(i).

The next observations of deposition were made using LLZTO. Two locations were prepared based on surface roughness: 200 and 4 nm. Gold electrodes were sputtered onto each of these surfaces of the solid electrolyte as a current collector and substrate for Li deposition. Constant current densities of 0.01, 0.1, 0.5, 1, and 5 mA cm^{-2} based on the surface area of gold sputtered were applied in 15 min intervals. Both locations reached a short circuit at the 1 or 5 mA cm^{-2} interval with no correlation between the rough or smooth surfaces. Li deposition is observed through LLZTO onto the gold substrate sputtered onto the 4 nm-surface-roughness solid electrolyte, where crack propagation and growth is observed about halfway through the cycle. Through this and other investigations *via* OM, the group shows that Li deposition occurs in the cracks

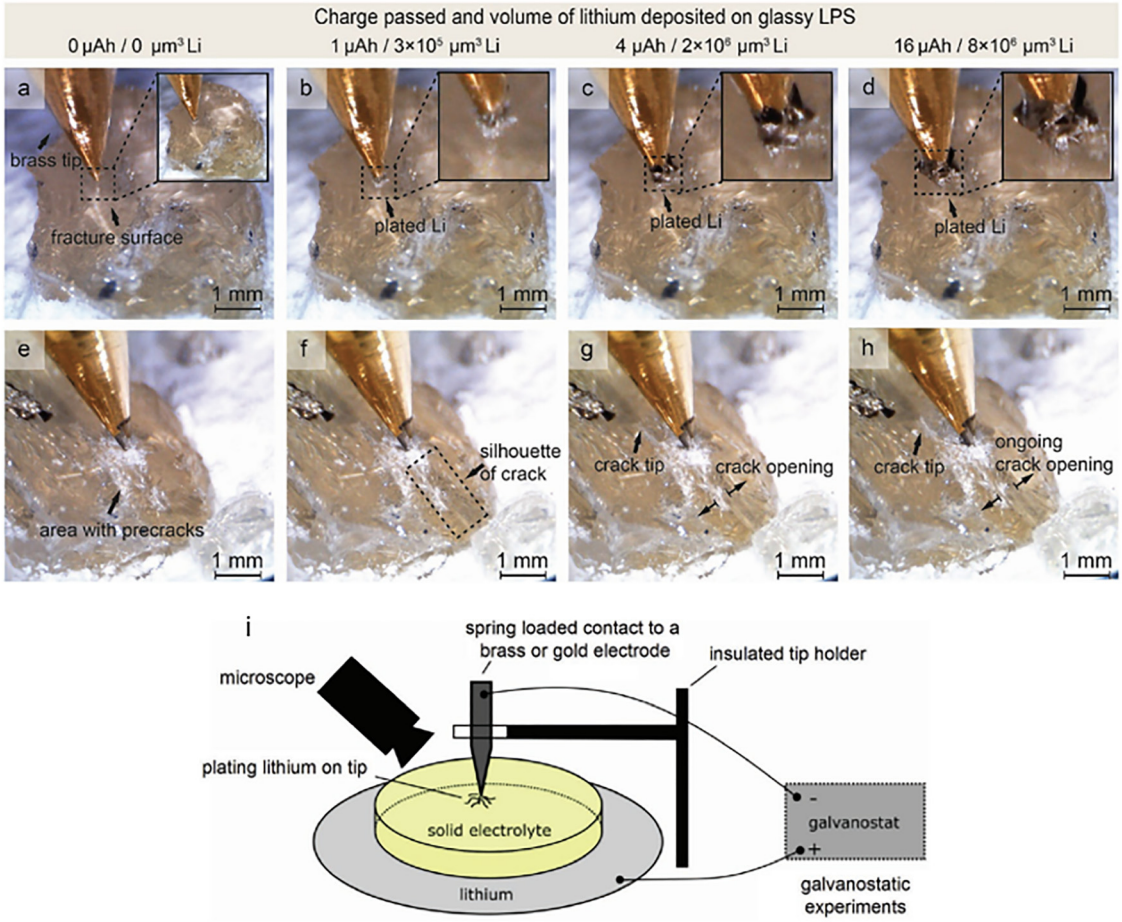

Fig. 6 OM images of Li deposition through glassy LPS on pristine and scratched surfaces after 0 μAh (a) and (e), 1 μAh (b) and (f), 4 μAh (c) and (g), and 16 μAh (d) and (h). (i) Schematic of point electrode and OM objective apparatus for observing Li deposition. Reprinted (adapted) with permission from ref. 19. Copyright (2017) John Wiley and Sons.

and that these cracks are responsible for shorting the cell although they cannot determine which one.

The group also observed Li penetration through polycrystalline β-Li_3PS_4 onto a brass point electrode similar the setup for glassy LPS. A high current density of 50 mA cm^{-2} was passed through the electrolyte based on tip electrode area for 2 min. Through transmission OM the group observed deposition inside the bulk of the electrolyte in a branching pattern and not on the surface of the point electrode. Upon SEM investigation of the solid electrolyte after deposition, the group observed a Li metal network along pore channels and grain boundaries of the solid electrolyte, further confirming the branching behavior of Li deposits.

These observations made *via in situ* OM show that the proposition by Monroe and Newman[9] is not necessarily true. Monroe and Newman proposed that dendrite propagation can be suppressed if the solid electrolyte (or separator in their words) has a shear modulus approximately twice that of Li. Li metal has a shear modulus of 4.2 GPa, LPS has a shear modulus of 8.3 GPa, and LLZTO has a shear modulus of 61 GPa, much higher than that of Li, yet Li deposition propagated and grew cracks in all solid electrolytes tested. Porz *et al.* proposes that surface defects are to blame and that, above a certain current density, overpotentials and mechanical stresses drive Li deposition to fill surface defects and eventually force them to expand and continue to be filled.[19]

2.3 *In situ* visualizing the protection effects of surface coatings

In addition to the afore-discussed studies investigating the intrinsic behaviors of Li plating/stripping processes in liquid and solid electrolytes, there are also efforts invested for addressing the challenges of LMAs. In this respect, Sandoval *et al.* studied Li stripping and plating dynamics on bare stainless steel (SS) current collectors, antimony (Sb)-coated SS current collectors, and silver (Ag)-coated SS current collectors, using two electrolytes: (1) the carbonate electrolyte of 1 M $LiPF_6$ in 1 : 1 (v/v) EC/DEC and (2) the ether electrolyte of 0.8 M lithium bis(trifluoromethanesulfonyl)imide (LiTFSI) in 8 : 2 (v/v) dioxolane/dimethoxyethane (DOL/DME).[20] The Sb and Ag thin films are 100 nm thick. The group revealed that the SS electrode requires a large nucleation overpotential while the Sb- and Ag-

coated SS needs lower nucleation overpotentials to deposit Li. In particular, they comparatively conducted *operando* OM observations on Li plating and stripping on bare SS and Ag-coated SS current collectors in the carbonate electrolyte at a current density of 4 mA cm^{-2}. They found that the Ag-coating layer delayed the occurrence of Li dendrites during the plating process and led to a more uniform stripping behavior. The work emphasized the importance of *operando* OM studies on differentiating Li stripping and plating dynamics due to the different current collectors.

To inhibit Li dendrites, very interestingly, Tang *et al.* developed an ion-conducting layer of Li_xSi on the top of Li foil.[21] They first deposited a layer of Si on Li foil using a radio frequency (RF)-magnetron sputtering system at room temperature. The Si-coated Li foil was then transferred to a glove box and heated to 250 °C with the production of a Li_xSi layer. Compared to the inhomogeneity of Li plating/stripping on the surface of bare Li foil, the Li foil capped by the Li_xSi alloying layer enabled uniform plating/stripping. In the study, they employed an *in situ* OM system and observed the electrochemical deposition of Li on the Li_xSi-coated and bare Li electrodes with a custom-made glass cell (Fig. 7(d)). The cell was assembled symmetrically with either two Li_xSi-coated Li electrodes or two bare Li electrodes (Fig. 7(c)). Under a current density of 1 mA cm^{-2}, Tang *et al.* revealed that the bare Li‖Li cell exhibited uneven and porous Li deposition with evident dendritic growth after 6 hours (Fig. 7(e)), while the Li_xSi-coated Li‖Li cell showed smooth and dense Li deposition even after 10 hours (Fig. 7(f)). The distinct deposition behaviors of the two cells were also reflected on their voltage profiles. The Li_xSi-coated Li‖Li cell showed a flat voltage profile while the bare Li‖Li cell exhibited an unstable voltage profile (Fig. 7(a)). Tang *et al.* further quantified the morphological evolutions of the Li deposition in the two cells (Fig. 7(b)) and the Li_xSi-coated Li‖Li cell had a much lower Li deposition thickness than that of the bare Li‖Li cell. This study demonstrated that ion-conducting coatings are promising for suppressing Li dendrites and SEI formation.

In another compelling study, Zhang *et al.* developed a novel three-dimensional (3D) porous host of Li, lithiophilic dendrite-like Li_3Mg_7, which are favorable to Li plating/stripping, delay the formation of Li dendrites, accommodate large volume change during Li plating/stripping, and avoid the parasitic reactions on the Li surface.[22] This beneficial 3D structure was realized through applying $MgBu_2$ (Bu = *n*-butyl) on the surface of Li foils. The reactions between $MgBu_2$ and Li foils at 200 °C

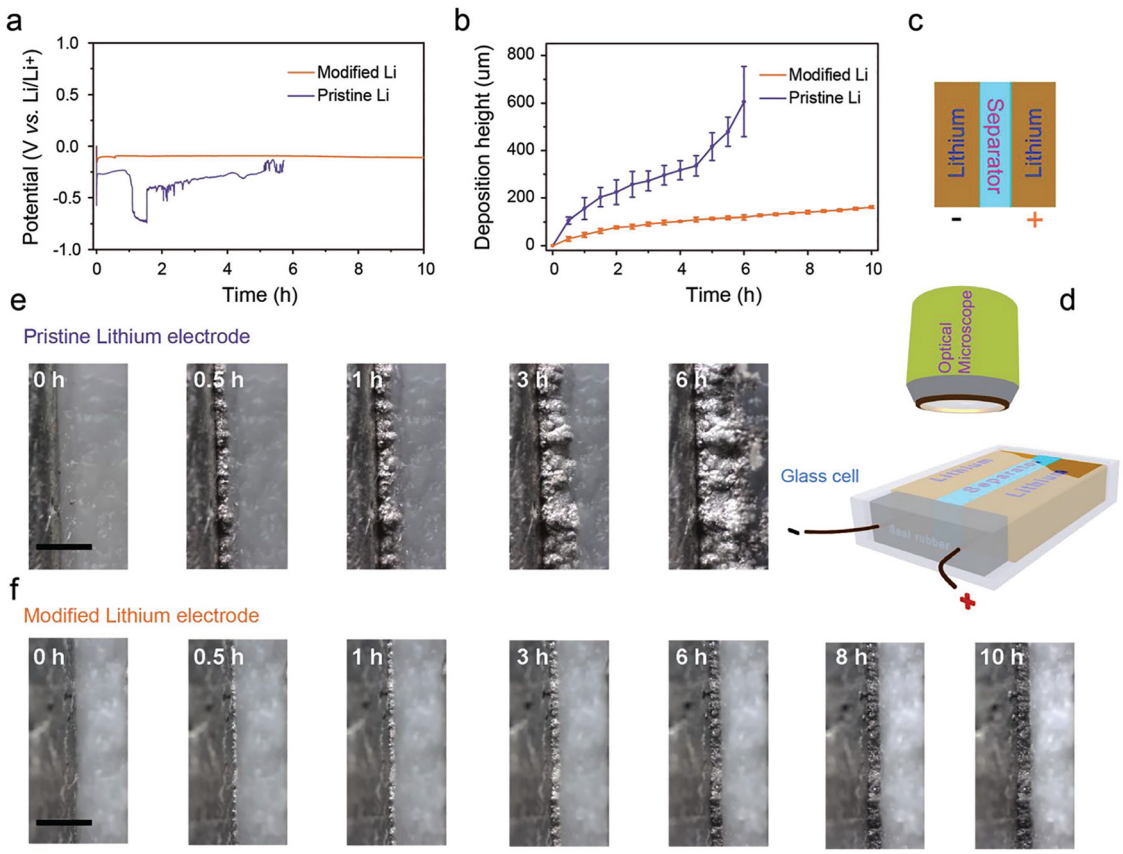

Fig. 7 *In situ* optical microscopy observations on Li electrochemical deposition. (a) Voltage profiles of Li deposition and (b) Li deposition thickness of the Li_xSi-coated and bare Li electrodes at a current density of 1 mA cm^{-2}. Illustrations of (c) the symmetric Li‖Li configuration and (d) the OM system with the glass cell. The Li deposition of (e) the bare Li‖Li cell and (f) the Li_xSi-coated Li‖Li cell. Reprinted (adapted) with permission from ref. 21. Copyright (2018) John Wiley and Sons.

led to dendrite-like Li_3Mg_7 enriched with Li-containing polymer and LiH decorated on Li foils. Using an *in situ* OM system, Zhang *et al.* clearly demonstrated that the Li_3Mg_7 structure efficiently inhibited SEI and Li dendrites from occurrence. Furthermore, Shi *et al.* also reported a distinct design of LMAs,[23] in which graphene nanoribbons (GNRs) were applied on Li foils while an SEI layer induced in the LiTFSI–ether electrolyte was grafted on the GNRs, leading to a protective layer of SEI@GNRs over Li foils. The resultant SEI@GNRs-coated LMAs exhibited excellent electrochemical performance in a $LiPF_6$-based carbonate electrolyte. Using an *in situ* OM system, Shi *et al.* visualized the continuous growth of a loose and porous Li layer in bare Li‖Li cells while the SEI@GNRs-coated Li‖Li cells produced a compact and smooth Li layer. This study demonstrated the combination of GNRs, and the LiTFSI-ether induced SEI is important, for GNRs have exceptional mechanical properties while the inorganic components of the SEI layer (LiF, Li_3N, and Li_2S) decrease the Li nucleation overpotential and make Li deposition and nucleation uniform. They jointly inhibited the formation of SEI and Li dendrites in the carbonate electrolyte.

All the afore-discussed studies demonstrated that *in situ* OM systems are valuable to visualize the evolutions of Li surfaces. Thus, they are an important tool to study Li plating/stripping behaviors and visualize the effectiveness of any tackling measures in a real-time mode.

3. SEM observations on the evolutions of Li dendrites

In situ SEM employs a focused electron beam to deliver high-resolution imaging, enabling direct observation of Li nucleation, deposition, and dissolution at the nanoscale.[24] This capability has been particularly important in visualizing short-circuiting mechanisms and the underlying causes of failure.[25] The *in situ* technique enables real-time monitoring of electrochemical processes under their natural operating conditions, providing insights that are difficult to obtain through conventional *ex situ* analysis.

Building on these capabilities, *in situ* SEM has been employed to investigate the fundamental difference in Li affinity among various substrate materials. Cui *et al.* directly observed Li deposition modes on 10 different metallic substrates using a solid polymer electrolyte (SPE) with LiTFSI salt, along with a tungsten probe.[26] On lithiophobic metals (Cu, Ti, Ni, Cr, and Bi), deposits were vertical and grew in a dendritic shape. Whiskers initially nucleated randomly then shaped into long and thin kinked dendrites, growing mostly from the root. Lithiophilic metals (In, Ag, Au, Pd, and Al) had lateral and particulate-like growth mechanisms that were uniform in both growth rate and shape. Instead of growing outwardly in dendritic fashion, their diameters gradually grew until the particles could merge and homogenously cover the entire substrate surface. Their growth rate was also much slower and steadier, discouraging erratic dendritic growth that results in short circuiting. These different behaviors are rooted within Li's solubility of these substrates. Lithiophobic metals like Cu cannot alloy with Li, thus the two metals will remain separate from each other. A period of no growth happens for the nucleation energy to accumulate until the energy barrier is overcome, different from materials that alloy easily with Li then spontaneously nucleate and grow on the surface. Reduced Li quickly dissolves into indium to form an alloy, facilitating a much higher nucleation density and very low overpotential during electrodeposition. A high affinity to Li and crystallographic compatibility with Li are considered to be important factors for an optimal substrate.

The varying substrate affinities with Li are considered a major dictator in the different deposition modes, shown by the time increments of Li growth during plating on Cu *versus* In substrates in Fig. 8(a) and (b). Highly lithiophilic In-type substrates easily form various Li–In alloy phases, allowing a wide solubility range where Li can dissolve when reduced. A spontaneous alloying process followed by low-energy nucleation and growth contributes to high nucleation density with very little overpotential. Li growth on this substrate is described as particulate and uniform, each of the nucleation particulates are a similar size, with a constant growth rate and increasing diameters in all directions. They keep their homogenous shape, soon merging with nearby particles to cover the entire substrate surface for more efficient and sustainable growth mechanics. In comparison, Li nucleation on the lithiophobic Cu substrate is ''slow and sluggish'' with low nucleation density, drawn through the insolubility and a rather large energy barrier. There is an incubation period where temperature builds until the barrier is overcome which can cause inefficient and unsustainable dendritic growth. The dendrites begin as short whiskers and grow from the root into long and needle-like structures. With an unchanging diameter, deformed kinking soon results, exaggerated by the later-formed whiskers pushing the older grown dendrites up and out of plane.

Lithiophilic substrates were further investigated by Leite, *et al.*, who conducted *in situ* SEM observations on all-solid-state LIBs with aluminum anodes to investigate capacity loss causes.[27] The batteries exhibited a 90% drop in capacity after 100 cycles, attributed to severe electrode degradation. During the first charge–discharge cycle, Li diffused into the Al thin film, reacting first with the Al_2O_3 surface layer, then with the underlying Al to form Li–Al–O alloys and alloyed mounds. This process exposed unoxidized Al beneath the oxide layer, creating a pathway for continued Li diffusion and sub-surface alloying. These initial alloyed regions expanded into small protrusions or mounds, which grew larger as adjacent sites merged, forming cracked boundaries. Although these mounds maintained electrical contact, they failed to dissolve during discharging as expected. The voids generated during alloying oxidized and obstructed diffusion pathways, leading to irreversible Li trapping within the immobile mounds, an effect that intensified with cycling. Consequently, Li became increasingly immobilized, while the anode's ability to expand and contract diminished after just one cycle. Efficient alloy formation required Li

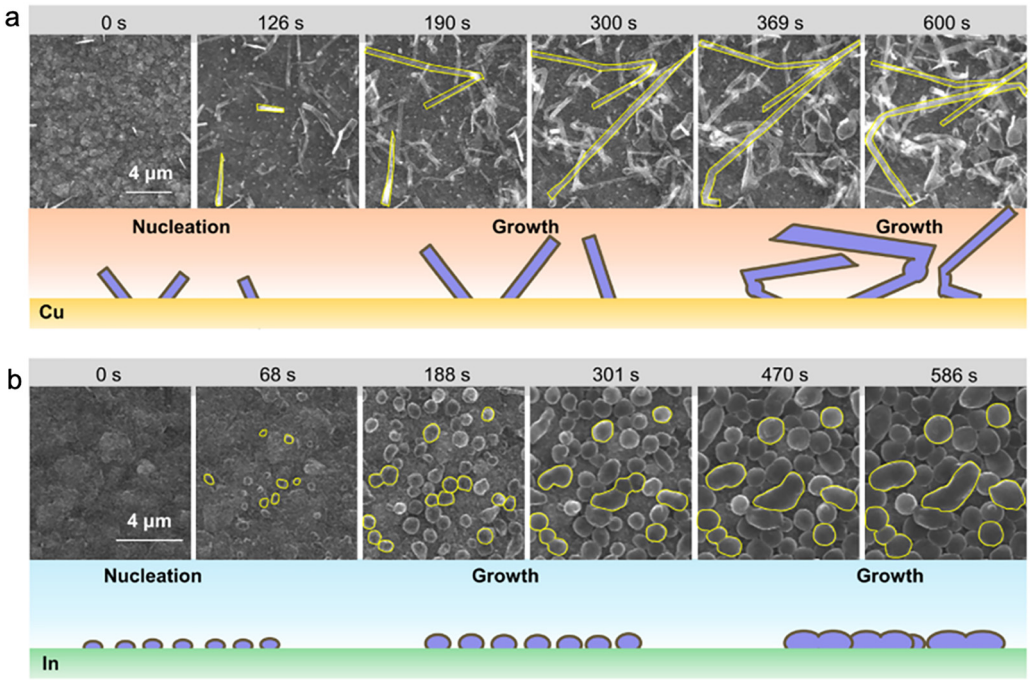

Fig. 8 SEM imaging and the growth model associated with the two different substrate types: (a) Cu or lithiophobic substrate materials *versus* (b) In or lithiophilic substrate materials.[26] Reprinted (adapted) with permission from ref. 26 under a Creative Commons Attribution (CC BY) license.

to diffuse through the underlying film and Al to diffuse outward to the growing mound, both diffusion steps subject to significant resistance. Continued cycling led to incomplete decomposition and residual, unusable Li on the surface. Using an inert metallic capping layer or modifying the anode surface are possible solutions to mitigate these surface-driven degradation mechanisms.

The interface between an electrode and an electrolyte is a critical component of battery performance but has previously been difficult to monitor during cycling. To reveal important information regarding their interactions, Golozar *et al.* performed *in situ* observations of Li plating and stripping for several days using cross-sectional SEM imaging.[28] They constructed an observable cell that included an $LiFePO_4$ (LFP) cathode and a SPE with LiTFSI as the main conductive salt. Li was deposited at increasing C-rates of 0.1 mA (C/12) during the first cycle, 0.403 mA (C/3) during the second through fifth cycle, 0.537 mA (C/2) during the sixth through 11th cycle, and 1.074 mA (1C) until failure. The images in Fig. 9(a)–(h) are taken of the Li anode and SPE interface throughout several stages of cycling. The first image displays smooth anode and interface edges, until several days of cycling continually changes the morphology. As cycling continues, increasing changes of the following are seen: dendrite growth on the anode edge, nucleation on grain boundaries (regions of relatively higher free energy and diffusion rates), isle formation on anode surfaces, and Li metal depletion close to these isles. The smooth electrode/electrolyte interface at the beginning quickly protrudes into the SPE after 13 hours of cycling, indicating an unstable interface where the absence of a SEI layer allows early dendrite formation.

After the first cycle, a uniform SEI layer stabilizes the interface, though more damage to this layer results in greater dendrite formation as the C-rate continues to increase with continual cycling. Anode edges and grain boundaries are the dominant nucleation sites, and isles appear shortly after the C-rate increases to C/2, forming a new edge on the Li surface. By the end of cycling, dendrites grew on the grain boundaries and newly opened edges, with severe Li depletion in the surrounding areas. Previously formed dendrites were also completely encapsulated by newly formed SEI compounds including Li oxides, carbides, and carbonates. Large amounts of Li were consumed to form these compounds, as well as to continue cycling to compensate for continual dead Li formation. Additionally, cracks and newly exposed grain boundaries required increased Li consumption, either from non-uniform SEI or non-homogeneous electrode/electrolyte contact. The temperature for this experiment was purposely increased from the stabilizing, initial temperature of 70 °C to a higher temperature of 80 °C to improve ionic conductivity after two days of cycling.

Further magnification of a view more focused on the SPE is captured in Fig. 9(i)–(n), with dendrite growth penetrating through the electrolyte, close to the anode edge. Electrolyte and SEI decomposition result in increased resistance and is likely the main factor behind the exothermic reactions increasing the local temperature at the electrode/electrolyte interface. The polymer regions in contact with the dendrites raises its temperature above the melting point causing a liquification and allowing continual penetrating growth. In addition to penetrating dendrites causing short circuiting, it can also elevate the overall battery temperature and lead to thermal runaway. An improved electrode/electrolyte interface stability is

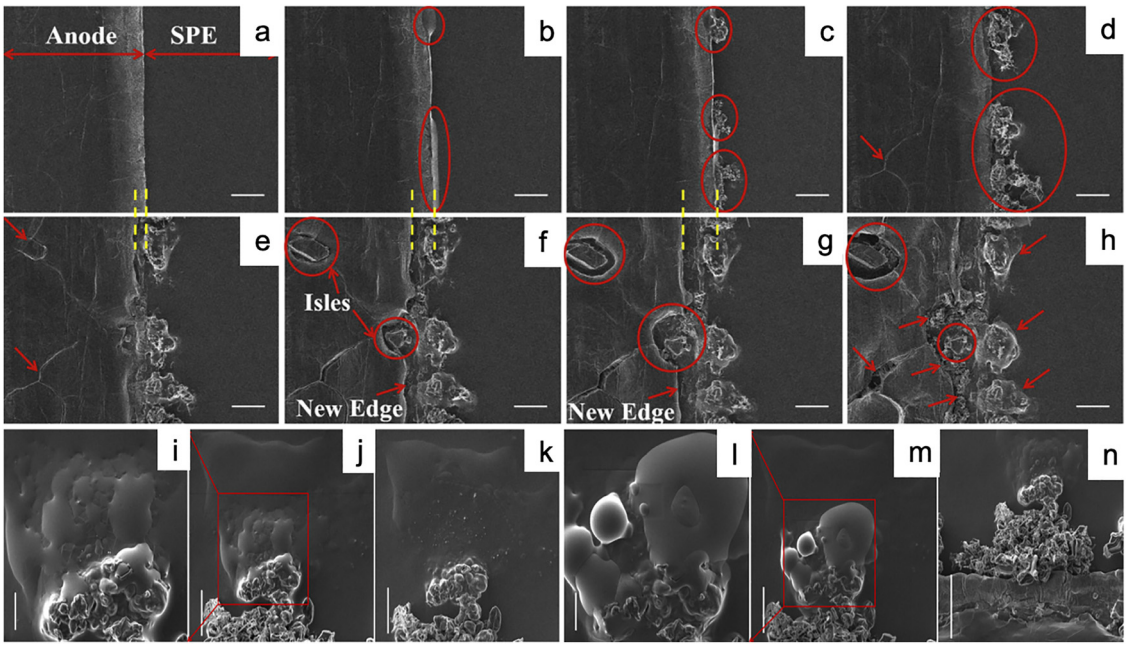

Fig. 9 (a)–(h) SEM images of the Li/SPE interface at various times during plating, showcasing interfacial deformation and the formation of isles and new edges. (i)–(n) SEM images showing dendrite perforation through the SPE and into contact with the cathode to short-circuit the cell.[28] Reprinted (adapted) with permission from ref. 28 under a Creative Commons Attribution (CC BY) license.

key to more stable and higher capacity electrochemical performance.

Found to be a recurring source for battery failure, Golozar *et al.* again used an *in situ* SEM setup, here to better understand the role of Li dendrite in short circuiting a battery.[29] Pure Li metal is too soft to penetrate SPEs themselves, but Li carbide and oxide compounds that rapidly form along with this growing metal increase the outer shell hardness. The carbon and oxygen contamination on the dendrite surfaces is sourced from both decomposition of the polymer SPE during cycling and environmental elements. Needle-like growth produced more carbon compounds compared to mossy dendrites, suggesting chemical and mechanical decomposition are a main factor for gas release from the electrolyte. Fig. 10(a)–(d) provide cross-sectional SEM images taken at varying time intervals during charge–discharge cycling. The first image was taken before cycling and clearly differentiates between the anode, electrolyte, and cathode. By the second image, there are cracks beginning to form on the anode and mild layer morphing. By the third and fourth images, which were taken after weeks of cycling, complete cracking and shifting of the three components are clearly visible. The anode and electrolyte shift apart, creating regions of high and low pressure between themselves. These turn into ideal locations for Li extrusions, apparent by the nonhomogeneous growth depicted in the images. As a result of the cell setup, pressure was only applied at the sides of the battery. Under low pressure, Li could more easily extrude and form needle-like dendrites, most notably along the edges of the anode or near surface defects. Fig. 10(e)–(h) show the plane-view SEM images of an additional experiment performed with no applied pressure. Most notable are the two needles on the top (anode edge), as they grow early on and move around throughout continued cycling. There is a 90-degree angle kept between the two needles the entire period; a sign the needles have a preferred orientation between each other. Li rods could be attached, indicating the growth was switching between growth from the tip, base, or other areas. Fig. 10(i)–(l) characterize a similar needle that was lifted off and milled after dissolution to reveal a hollow structure with a thin shell. Starting at later formed areas with a thinner SEI layer, these needle structures left behind SEI residue shells measured to be around 100 nm. There remained an inactive dead Li tip that was electrically separated from the surface, suggesting the thin shells are also very brittle. The driving force of continual Li deposition that is encapsulated by a hard outer shell can penetrate and decompose the SPE before leaving behind unusable Li.

Bulk-type electrolytes have been proven to exhibit a high capacity but are susceptible to dendritic Li penetration. Their inorganic SE has eliminated Li metal reactant elements, while maintaining the high Li-ion conductivity and chemical stability. Nagao *et al.* investigated Li behaviors in bulk-type all-solid-state cells using the sulfide-based electrolyte Li_2S–P_2S_5.[30] An *in situ* SEM setup observed Li deposition and dissolution at the SE/stainless-steel CC interface at a relatively high current density of 2 mA cm^{-2}. Images were taken before cycling (Fig. 10m), after 10 minutes (Fig. 10n), and after 32 minutes when the cell short circuits (Fig. 10o). SEM images of the solid electrolyte and Li anode interface show the distance between the SS and SE expands and the SE surface becomes more rugged, and pillared structures form and grow.

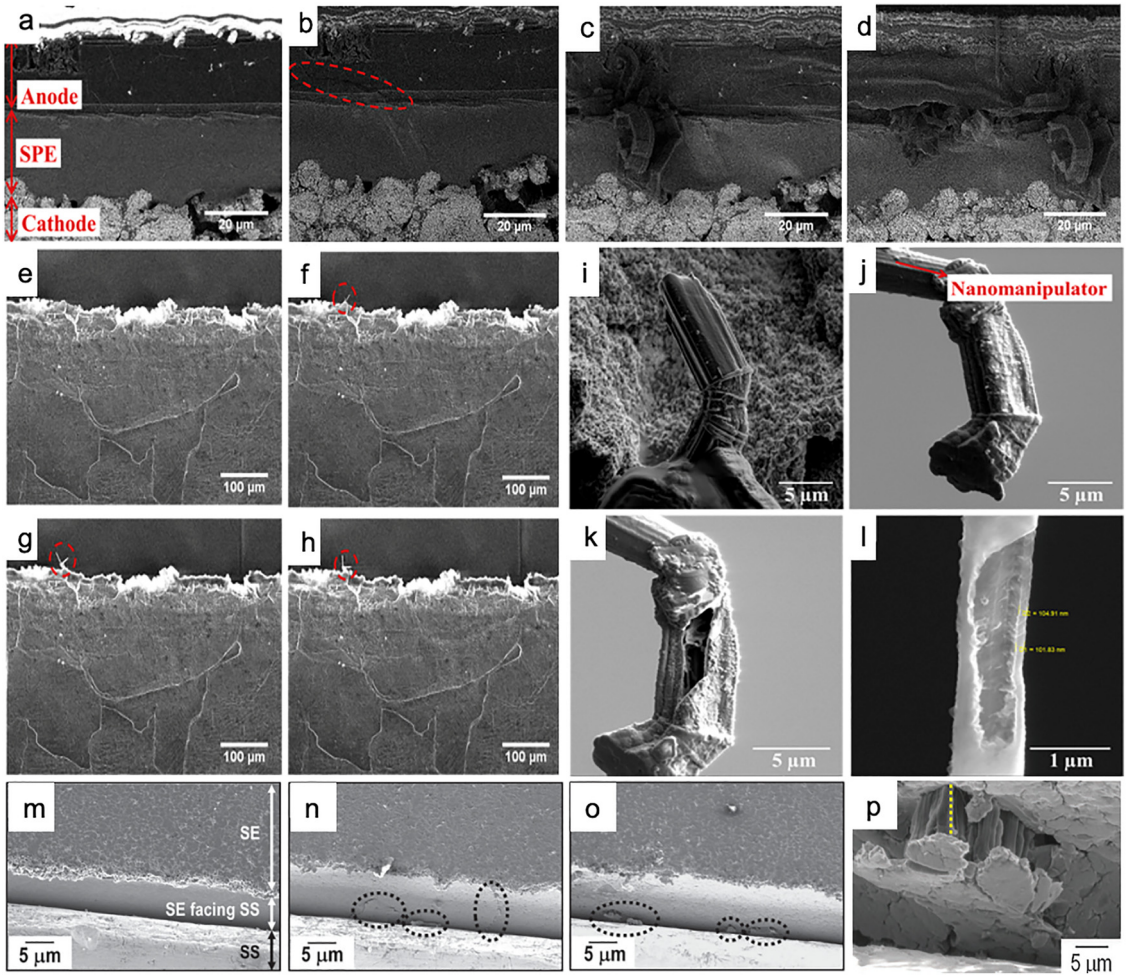

Fig. 10 (a)–(d) Full-cell cross-sectional SEM images of the anode, SPE, and cathode interfaces. Images were captured at four different times: before cycling, after 3 days, after 13 days, and after 16 days and the last cycle. (e)–(h) Cross-sectional SEM images of the anode/electrolyte interface. Images were captured at the same four times as parts (a)–(d). (i)–(l) SEM images showing dendrite formed on the anode, dendrite detached, FIB image displaying a hollow structure, and measured dendrite wall thickness.[29] (m)–(o) SEM observations at the SE/SS interface (m) before cycling, then after (n) 600 s and (o) 1920 s of Li deposition. (p) SE/SS interface in the same cell immediately after short circuiting.[30] Reprinted (adapted) with permission from ref. 29. Copyright (2018) American Chemical Society. Reprinted (adapted) with permission from ref. 30. Copyright (2013) American Chemical Society.

Before deposition, the SE appears with no cracks, and a smooth CC/electrolyte interface is featured. Then, Li initially deposits along or in the vicinity of grain boundaries, but after only 10 minutes some prominent cracks already appeared and Li proceeds to only nucleate around these areas. New cracks or deposition sites are rare after this stage, as Li exclusively deposits along SE/SS contact areas and already formed cracks. Since expansion and contraction at the electrode–electrolyte interface during cycling is expected, continual Li plating and stripping increases and decreases the surface area of these contacted sections. More specifically, the electrode and solid electrolyte move further apart as Li deposits onto the stainless-steel CC. The reverse action occurs as Li dissolves back into the electrolyte. Thus, the increasing distance between the electrode and SE resulted in elongated cracks and pillared Li structures, ultimately leading to short circuiting after 32 minutes, further imaged in Fig. 10p. It should be noted that since this cell was designed for *in situ* SEM observations, insufficient pressure was applied, which increased the resistance and slightly changed the deposition morphology.

Of the many failure mechanisms harming Li deposition ability, electrode cracking is another major issue associated with Li metal anodes. Zhao, *et al.* reported on possible causes of Li induced cracking, using a focused ion beam-SEM (FIB-SEM) to observe *in situ* Li deposition onto garnet SEs.[31] In ceramic LLZTO, Li deposition causes a higher amount of transgranular cracking, through the grains, compared to inter-granular cracking, along grain boundaries. LLZTO is brittle for a SE, so once a crack forms it can very quickly expand and extend, causing more pressure on other grains. The resulting expansion travels to the surface, leaving a bowl-shaped crack that lifts away and eventually completely detaches the Li piece.

To further understand the causes behind this mechanism, Fig. 11(a) shows sequential SEM images during several stages of cycling, with the full bowl-shaped crack on the left and their further magnified images on the right. Starting from a small

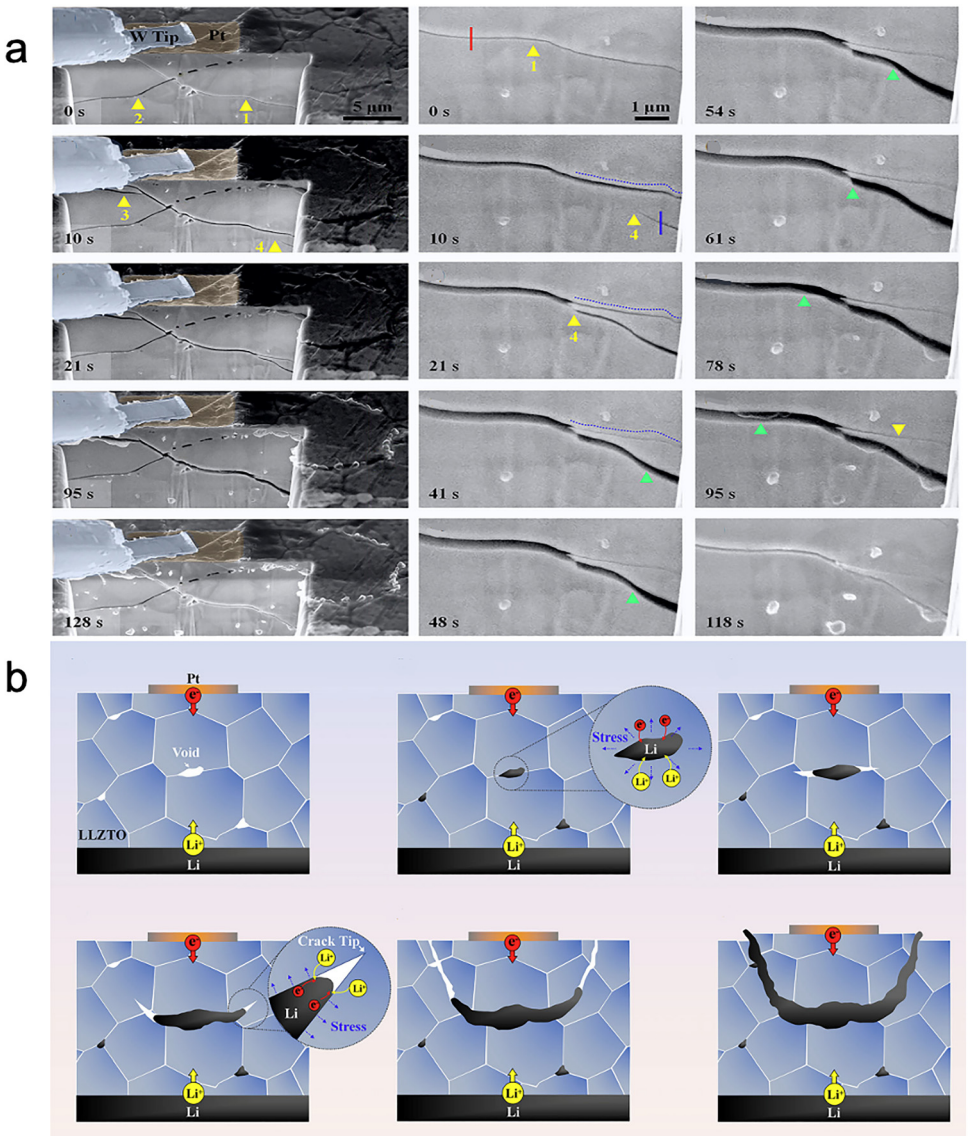

Fig. 11 (a) *In situ* observations of a crack evolution after several minutes of Li deposition. Arrows marked 1–4 indicate various cracks formed during this process. Different cracks are labeled and numbered with yellow arrows, while Li filling into the spaces is indicated with a green arrow. (b) Schematic representing a small defect forming then increasingly filled with deposited Li to produce wedging stresses and a disconnected bowl-shaped section from the surface. Reprinted (adapted) with permission from ref. 31. Copyright (2021) Wiley John and Sons.

defect or void underneath the surface, Li can seep through the cracks and deposit within the small opening. Continual Li flowing through these cracks causes increasing internal stresses across the entire SE that can enlarge, disform, or create entirely new cracks. Cracks start off short and thin, but continued time and increased voltage create a cycle that thickens, lengthens, and merges the cracks. In the figure, crack 4 branches off from crack 1 and widens over time, though this causes both a compression of crack 1 as well as the branching of a new crack further away. Increasing Li volume generates greater localized pressure, and deposition sites along cracks and larger grain boundaries collectively force increasing expansion. By the end, an especially elongated crack disconnects several grains from the surface and lifts a bowl-shaped crack of which Li has filled entirely, illustrated in Fig. 11b. Upon reversing the potential and beginning stripping, Li at the surface is dissolved first and the openings remaining contract. The Li left prohibits complete healing after this step and lose electrical contact, leaving more dead Li that further break off dendrites and produce more dead Li with continued cycling.

An effective method for simulating Li dendrite behavior utilizes a thin Cu film as an anode, allowing direct observation of Li plating and stripping on a solid Li phosphorus oxynitride (LiPON) glass electrolyte. This setup is referred to as ''anode-free'' because during the first charging step, Li is deposited at the Cu CC/LiPON interface to produce the initial Li anode. Dendrite growth is observed originating at the LiPON/Cu interface, where it extends upwards and eventually bursts through

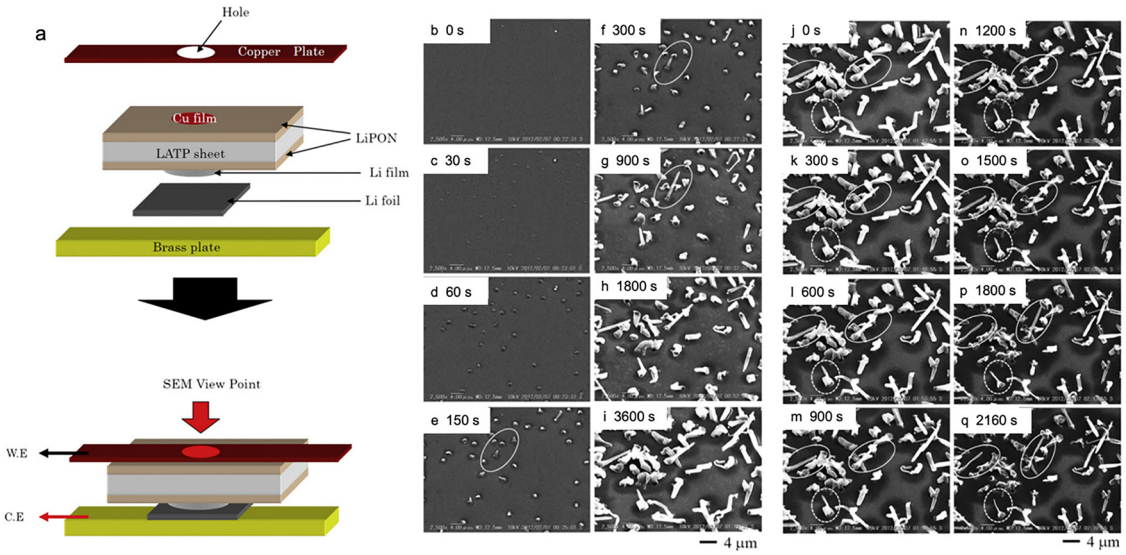

Fig. 12 (a) Cell configuration allowing *in situ* SEM visualization and imaging. SEM images taken through the thin Cu film observing dendrite (b)–(i) growth during plating and (j)–(q) shrinkage during stripping. Reprinted (adapted) with permission from ref. 32. Copyright (2013) Elsevier.

the thin Cu layer. The SEM viewpoint focused on this interface as Li deposits upwards through the thin Cu film, the dendrite breakthrough visible through a hole on the top side of the sample. A common experimental cell configuration, demonstrated by Sagane *et al.* in Fig. 12(a) involves using Cu and brass plates as the working and counter electrodes, respectively.[32] Since LiPON is amorphous and lacks grain boundaries, all surface sites have equal probability of serving as nucleation points for Li deposition.

In situ SEM images are shown of plating (Fig. 12(b)–(i)) then stripping (Fig. 12(j) and (q)) onto the Cu/LiPON interface. During plating, the initial nucleations are flat, with small islands of growths that uniformly trend in a lateral growth direction. After 150 s (d), Li evidently reached a height tall enough to break through the Cu film, then began to grow as rods in the vertical direction. As this process begins, newly precipitated Li is rarely observed, and it dominantly plates at the already plated regions. Because deposited Li is pure Li metal, it easily reacted with residual gas molecules (O_2 and H_2O) in the SEM chamber, forming a native layer of Li compounds on the surface of the deposits. The outside covering of these dendrites consistent mainly of Li_2O and LiOH, though several other additional gases are present to produce a heterogenous SEI compound layer.

During the stripping process, the Li rods gradually lose their metallic core and leave behind shells of Li reacted compounds. These precipitated dendrites appear "deflated" with thin, translucent, and fragile structures. The observed stripping mode for longer-grown dendrites is where Li precipitates from the bottom, leaving a solid metallic Li head that remains attached along with the SEI shells. Without an applied pressure to ensure uniform Li plating and stripping, the dendrites' roots are quickly taken first, leaving a broken electric connection between the CC and the majority of the plated Li. This is observed in the *in situ* SEM stripping images, as many hollow shells remain, with the particularly long dendrites having a solid tip that is classified as unrecyclable dead Li. A relatively low current density of 50 μA cm^{-2} is used for both the plating and stripping process, contributing to the sparse nucleation sites and dendritic growth mode.

Also utilizing an *in situ* LiPON/Cu cell with a viewpoint hole through thin Cu film, Motoyama *et al.* determined a greater number of Li nucleation sites are a direct result of higher current densities.[33] Below 300 μA cm^{-2}, the Li nucleation density is significantly smaller and allows separate Li growth, described as islands. If the nucleated Li does not coalesce before the local stress overwhelms the Cu layer strength, the surface will crack quickly without merging into a homogenous growth layer. Once perforated through the deformed Cu layer, they preferentially grow through the cracks and dominantly continue as rods. Since the total charge was held constant for all current densities, the overall amount of deposited Li was the same. However, at higher current densities, the nucleation density increases, and the amount of Li deposited per site is lower, leading to smaller individual islands that are more likely to coalesce into a continuous film due to their closer spacing. Lateral growth in all directions also continued longer while avoiding growing enough vertically to pierce the pressurized film.

In situ SEM images and the different growth mechanisms for high and low current densities in Fig. 13 display this concept nicely. During Li plating at 50 μA cm^{-2}, pictured in Fig. 13(a), a secluded nucleation bulge in the film appeared after 5–10 minutes, then the Cu surface cracked by the 15-minute segment. One-dimensional rod growth, modeled in Fig. 13(c), started from the breakthrough Li after piercing the Cu thin film, as no additional pressure energetically favored this site to continue growing. No new nucleation sites formed, and

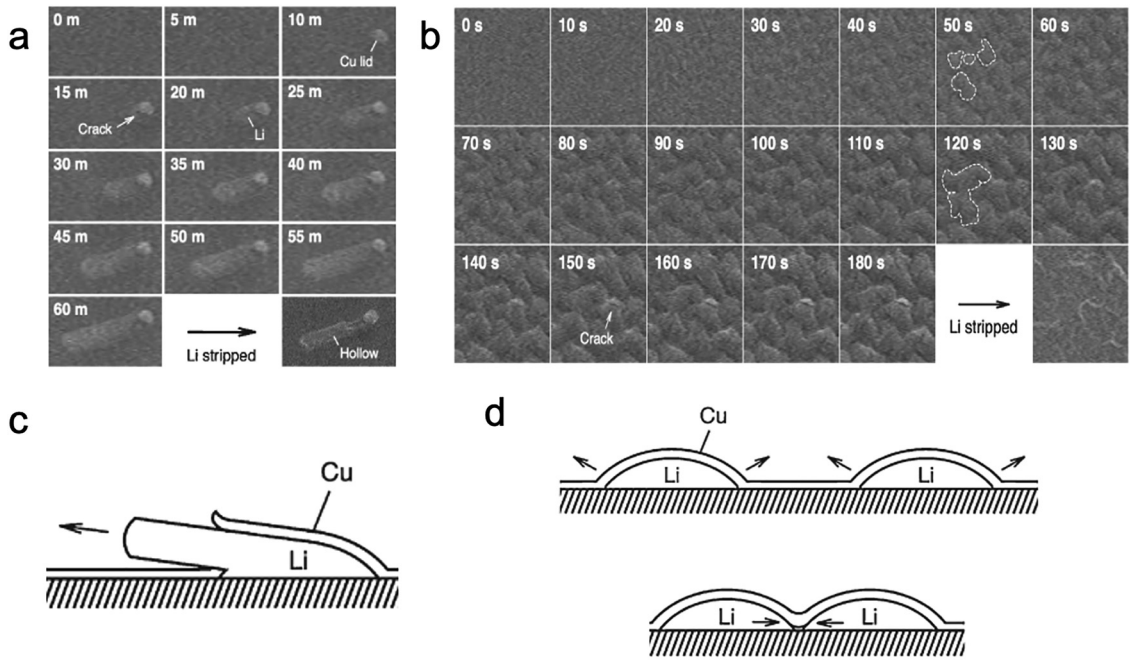

Fig. 13 SEM images and the corresponding growth models during Li deposition onto Cu/LiPON and after dissolution under (a) and (c) low current density and (b), (d) high current density.[33] Reprinted (adapted) with permission from ref. 33. Copyright (2014) The Electrochemical Society of Japan.

stripping left a hollow SEI shell and dead Li from the rod dendrite. In comparison, SEM images and the growth model of Li plating at 1 mA cm^{-2} shown in Fig. 13(b) and (d) showcase a distinct pattern of lateral expansion and depositing Li relatively uniformly. The Cu film does not experience its first crack until the 150 second mark, much further into the deposition process than with lower current density. Mounds will merge if they are in the same vicinity and the model visualizes how a greater number of nucleation points is advantageous for this behavior. Higher nucleation density and the lengthened time of lateral growth before film perforation are both key factors in uniform deposition across the entire interface.

Aiming to investigate the broader mechanical properties and failures through several full charge–discharge cycles, Motoyama, *et al.* performed Li plating and stripping onto the LiPON/Cu thin film interface under different pressure levels.[34] Cu film thicknesses of 30 nm and 1.0 μm were tested at 1.0 mA cm^{-2}, simulating applied mechanical pressures during cycling. With the thinner 30 nm-thick Cu film, Li repeatedly nucleated at existing sites where the Cu film was preciously cracked, the mechanical pressure exhibited by the film in these locations being minimized. Several film locations protrude during the first plating cycle, cracks formed along the boundaries of these domes, then Li preferentially plated during repeated plating/stripping within those cracks. SEI shells and dead Li continues to build throughout continued cycling. As a result, small Li residues remained at cracked regions during dissolution from the formation of surface compounds such as Li_2O and LiOH. Improved from the continually worsened deformations beginning at the first plating cycle from the thin film, the thicker 1.0 μm Cu film did not exhibit any significant changes or obvious cracks. Due to the much lower volume of Li plated with each charge, there was a reduced strain applied to the Cu film, especially compared with that required to crack the much thicker film. Thus, the parts of the film that did not significantly fracture displayed no preferred nucleation sites other than the already existing cracks and grain boundaries. These observations confirm that higher pressure applied to a surface produces confined lateral Li growth with more uniform and reversible formations.

Another experiment performed by Motoyama, *et al.* utilized a similar setup, though electrodeposited Li onto a platinum CC instead of Cu.[35] As a lithiophilic substrate, Pt alloyed with Li to form various Li–Pt alloy phase compositions, reaching a maximum Li amount at Li_2Pt. After the first appearance of dome-shaped nucleation points formed underneath the Pt CC, no observable cracks were exhibited during Li growth, improved from thin Cu CC films that frequently cracked along the deposited boundaries. When the surface supersaturated and the alloy penetrated the film, it diffused vertically through grain boundaries and the newly formed film surface cracks. After this point, dome diameters remained practically unchanged, as Li is deposited exclusively through these holes and formed no new nucleation sites. At larger current densities, Li concentration reached a point of supersaturation quicker, while the size of each Li particle decreased. Pt CCs allow for higher nucleation density and lower overpotential compared to Cu CCs, due to the reduced interfacial energy and softened Li–Pt alloy.

While nucleation density and Cu film pressure are defining factors during these experiments, outside oxygen pressure also significantly contributes to nucleation and dendrite growth styles. Yulaev *et al.* used an *operando* ultrahigh vacuum-SEM

(UHV-SEM) to investigate the effects of varying oxygen pressure levels on Li plating and stripping behaviors.[36] Using LiPON electrolyte and a $LiCoO_2$ cathode, they observed different formations of particles, nanowires, and large whiskers at three controlled oxygen pressure levels. Increased oxygen pressure allowed more rapid oxide formation that influenced in-plane Li surface diffusion, determining an increased charging rate led to a higher Li nucleation density and thus more uniform growth. Fig. 14(a)–(c) compare SEM images, growth models, and simulated particle growths under three different levels of oxygen pressure after one galvanostatic Li plating cycle at 0.77 mA cm^{-2}. On the left, the lowest pressure level (5.7×10^{-7} Pa) yields primarily 3D growth that continually stays in plane. The majority of Li plated is relatively large and does not cluster with each other, though displays minimal nanowire, out-of-plane growth. When pressure is increased by one magnitude (5.7×10^{-6} Pa), nanowires are the dominant growth mode, creating long, thin dendrites with very low nucleation density. Particle growth only occurs at the dendrite base, constantly creating additional particle surfaces to be oxidized, encouraging continually quick vertical growth. At the highest level of oxygen pressure tested (4.8×10^{-5} Pa), oxide formations are overwhelming, continually allowing new growth spots on the surface. They surround the entire area to create compressive stress with high growth impedance, promoting far more lateral growth and tripling the nucleation density.

The cross-sectional and top-view SEM images in Fig. 14(d)–(g) capture Li dendrite growth after charging and discharging at the intermediate oxygen pressure of 5.7×10^{-6} Pa. Li ions diffuse much quicker than oxygen can react, creating oxide layers of only around tens of nanometers that are stretched very thin on the newly formed metallic Li. Growth then only occurs through the base, as the activation energy around this area is still lower than at the surface, making new Li surface diffusion thermodynamically unlikely. Thus, rapid growth through already formed dendrites continues, creating dendrites with small diameters that are predominantly grown in the vertical direction. Kinks are natural, and as such the structures lack the mechanical strength to retain their shape. When discharging, the metallic Li dissolves through voids in the dendrite and these thin Li-oxide shells are all that remain. This is compared to the higher oxygen pressures where bulky oxide layers easily form to compress Li deposition/dissolution for uniform surface diffusion. This experiment further demonstrates the impact of surface oxidation rate on nucleation patterns and confirms the oxygen pressure effects suggested in Fig. 14(a).

$Li_7La_3O_{12}Zr_2$ (LLZ or LLZO) and similar materials as solid electrolytes have proven to exhibit a higher Li^+ conductivity than that of LiPON and are far more rigid than Li_2S–P_2S_5.[37] It also has a Young's modulus (modulus of elasticity) greater than the theoretical value of preventing dendritic Li growth, though continue to experience short circuiting from gradually increased cell voltage.[38] One established method has been to heat LLZ in dry argon gas to remove Li_2CO_3 and LiOH, compounds that easily form in air and have been thought to only have exchange reactions between H^+ and Li^+ in aqueous solutions. However, this method causes large interfacial resistance and commonly degrades the surface affinity of Li and LLZO.

By using a mechanical polishing treatment by HCl aqueous etching in air instead of an inert gas atmosphere, Motoyama, *et al.* aimed to create a lower resistance LLZ/Li surface layer.[37] They effectively etched Ta-doped LLZ (LLZT) in aqueous acid HCl, realizing the electrochemical activity of the inert compounds and a smaller contact angle between molten Li and LLZ. HCl etched LLZT pellets 0.5 mm thick were manufactured for this experiment by immersing them into 1.0 M HCl aqueous solutions for 5 minutes, named ''5 m-HCl-etched LLZT''. The pellets etched using this method found an increased stability limit through extended cycling through a 30 nm thick Cu CC film at 100 μA cm^{-2}, observed using *in situ* SEM. Unmanipulated, polished, and etched LLZT were tested and compared under the same conditions. Mechanical polishing was abrasive, leaving a significant number of defects with a coarse surface, leaving the LLZT grains left either exposed or pulverized into non-uniform LLZT layers. However, Li whiskers subsequently grew not only on LLZT grain boundaries, but evenly on grain boundaries and polished surfaces. With a greater nucleation site number density, local current density was significantly reduced, effectively avoiding short circuiting. By purposefully manipulating the substrate surface by etching instead of polishing flat grains, the nucleation sites increase, and local stress was decreased across several points.

To better differentiate the Li metal growth behaviors between glass, solid electrolytes and liquid electrolytes, Krauskopf, *et al.* deposited Li metal onto an LLZO solid electrolyte/Cu CC interface.[39] Since polishing LLZO usually leaves some surface roughness as well as hydroxides and carbonates, they used solid electrolyte that was freshly broken, resulting in a well-defined surface with distinct topographic contrasts. Electrodepositing by controlled electron injection, Li was plated and stripped at 500 μA cm^{-2} and 200 μA cm^{-2}, respectively. The Li in Fig. 15(a) mostly deposit onto a flat region showing a single grain boundary, the dominant nucleation site seemingly along or near this boundary. To further determine the structural effects of nonhomogeneous regions, Fig. 15(b) captures deposition in a region with several ledges and grain boundaries present. In agreement with the first site, nucleation is fast and plentiful around these sites while the flat sections are delayed and minimal. Images depicted in Fig. 15(c) provide a gradation curve correction for a highly contrasted image of those in the Fig. 15(b) deposition, highlighting how Li predominantly nucleates at grain boundaries and stark topological features.

In a later experiment, Krauskopf *et al.* observed the Li metal and inorganic solid electrolyte LLZO interface during Li deposition utilizing a tungsten needle as an *in situ* microelectrode.[41] The glassy LLZO is atomically smooth, enabling ultrafast charge transfer kinetics that are usually affected by contamination layers or damage *via* polishing. Short circuiting happened easily, due to Li growing both through cracks in the ceramic solid electrolyte and laterally along its surface, as shown by

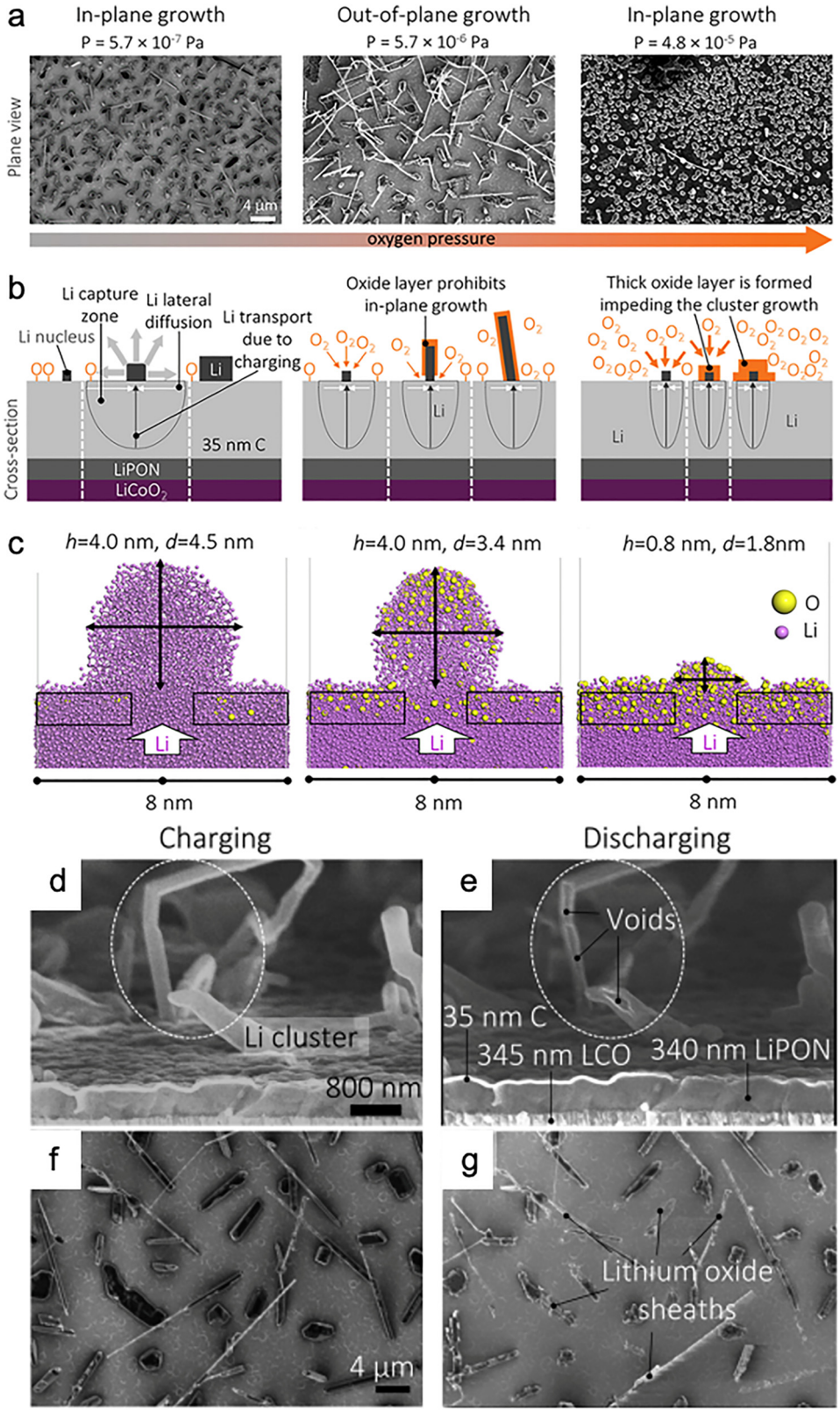

Fig. 14 A schematic of increasing oxygen pressure effects on Li growth size and shape. Row (a) compares plane view SEM images, row (b) visualizes cross-sectional dendrite growth, and row (c) portrays Li growth size differences. Top-view (d) and (e) and cross-sectional (f) and (g) SEM images during both charging and discharging at an oxygen pressure of 5.7×10^{-6} Pa. Li oxide shells can be seen after Li is stripped, including the voids where it broke and the remaining shells. Reprinted (adapted) with permission from ref. 36. Copyright (2018) American Chemical Society.

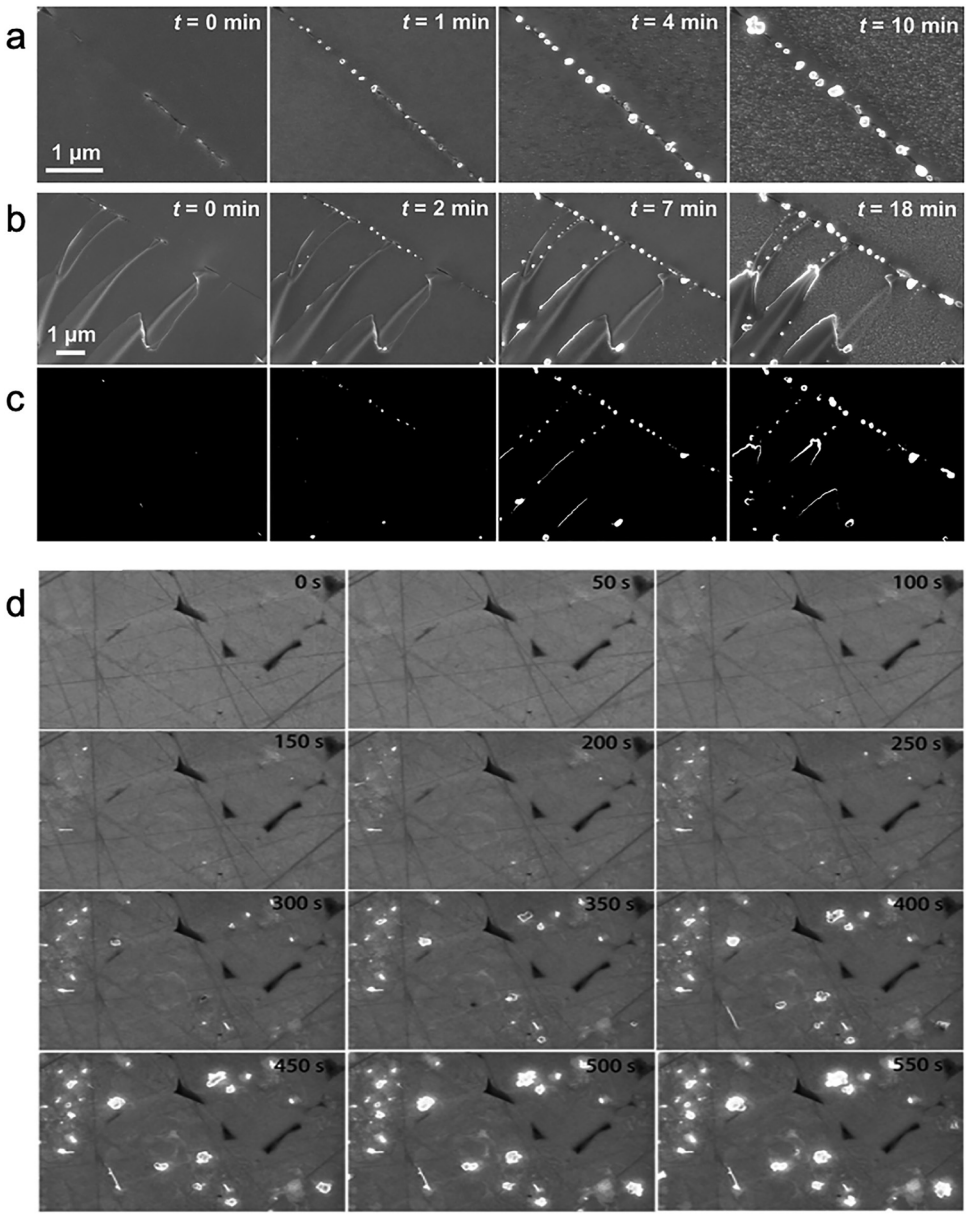

Fig. 15 SEM images during Li deposition at various locations and current densities. (a) 500 μA cm^{-2} at a relatively smooth location with one grain boundary. (b) 200 μA cm^{-2} at a more topologically diverse location. (c) Images from (b) after a manual gradation curve correction to better distinguish the Li metal and substrate.[39] (d) SEM images captured of Li deposition onto LLZTO at 50 s intervals. Deposited Li is shown as bright spots, further illuminated to better distinguish the contrast.[40] Reprinted (adapted) with permission from ref. 39. Copyright (2019) American Chemical Society. Reprinted (adapted) with permission from ref. 40. Copyright (2014) Elsevier.

SEM images taken during different time intervals within several minutes of the beginning of deposition. Overpotential gradually increases by −1 V every 30 s, while current increases exponentially over time as the interfacial contact area expands. At low overpotentials, the current remains consistent, evident by stable vertical Li plating with no changes to the interfacial contact area. As overpotential and current both increase with time, Li also grows laterally, likely due to several reasons. First, dislocations or other defects could minimally be present on the smooth surface of LLZO. Also, the tungsten needle tip is believed to have caused local mechanical stress and deformation of lithium. This has been attributed to the electric field distribution change close to the microelectrode. They noted in their previous experiments that these actions could be equally observed across the entire LLZO substrate.

To measure and control the important effects of beam irradiation on LLZTO, Xie, *et al.* aimed the SEM electron beam at the surface, which penetrated into the bulk LLZTO and expulsed materials from the surface.[40] In order to initiate a strong expulsion, the electron beam must build up the electric field to a certain strength, meaning a longer time and period of accumulation to achieve a stronger beam. Li ions have very

high mobility in electrolyte, making them the primary element to be ejected and then easily reduced by the surplus of electrons from the beam to be detected. The internal electron field attracts Li ions from the electrolyte, providing insight into ion behaviors and Li growth. Using SEM, the images in Fig. 15(d) captured Li expulsion from LLZTO every 50 seconds. Interestingly, expulsion of Li does not occur at the grain boundaries, but instead from inside the grains. These areas that normally are hotspots for Li growth are starkly contrasted in black on the images, indicating no Li observable expulsion. As with the ejected Li, they found that there was a direct correlation between expulsed Li accumulation rates and growth rates. An earlier formed group tends to slowly accumulate, while a delayed start of growth in an area often results in faster and larger expulsions. This is especially true for the last group, as a sudden ejection exceeds the frame recording rate, as visualized by their sudden appearance and continued rapid growth. The behavior of Li under beam irradiation shares notable similarities to Li metal dendrite growth mechanisms during electrochemical cycling. Instead of a penetrating electron beam that expulses ions through an internal electric field in this experiment, Li dendrites are formed in batteries by the ionic polarization at the electrode/electrolyte interface under an applied current. Although the driving forces differ, this beam irradiation experiment offers valuable insight into nucleation behavior and morphology evolution, particularly on well-characterized deposition substrates.

Overall, *in situ* SEM has proven to be a powerful tool for probing and observing Li metal mechanisms during battery operation. Compared to other *in situ* imaging techniques that observe Li dendrite growth, SEM provides great spatial resolution, operational flexibility, and compatibility within various environments.[24] However, the influence of the electron beam must be regarded, as prolonged or intense beam exposure can have destructive effects.[40] The nucleation density of the observed regions is often different from the regions outside the field of view.[32] Despite these limitations, *in situ* SEM eliminates the need for disassembly or vacuum removal, which can easily damage the fragile Li structure, and enables real-time imaging in the original sample experimental position.

4. TEM observations on the evolution of Li dendrites

The primary benefit to using a TEM for *in situ* or *operando* observations is its very high resolution, often <0.2 nm. However, the challenges associated with high magnification include the requirement of a vacuum environment, as the electron beam will lose clarity if it must travel through an environment with gas or air molecules, so the sample chamber is held at a very low pressure. Because Li cycling is carried out through an electrolyte, either liquid or solid, novel cells are created to house the electrolyte and electrodes inside the vacuum TEM chamber for *in situ* investigation. Generally, for TEM investigations, those cells are either an open or closed cell configuration. An open cell is dry and was used to investigate lithiation of individual carbon nanotubes,[42] silicon nanowires,[43] and other nanostructures, where the structures under investigation are touched to the surface of a Li metal counter electrode and the native layer present on the metal is used as a solid electrolyte. Although these investigations reveal mechanisms of lithiation and the development of SEI on the surfaces of those structures imaged, they do not offer electrolyte-specific mechanisms that are directly applicable to future LMB applications. For this reason, the following discussion will focus on closed-cell configurations, where commonly used electrolytes submerge the electrode under investigation, and more applicable findings are discussed.

Leenheer *et al.* designed a novel TEM liquid cell with a small enough working electrode such that it could be observed in its entirety at submicron resolution.[44] The cell uses SiN_x membrane windows and 1 M $LiPF_6$ in 1 : 1 EC : DMC electrolyte with tungsten working electrodes. Ten working electrodes were deposited onto a substrate and were masked with Al_2O_3 except for a small square area of 0.26 μm^2, this unmasked area notated by the green outline in Fig. 16(a) is the active Ti working electrode where Li deposition takes place. Because ten of these areas were deposited, ten experiments can be carried out without having to disassemble or otherwise disturb the cell. The first *in situ* observation and experiment through two full cycles are depicted in Fig. 16 below, including the overpotential and current profiles (Fig. 16(b)).

Two full plating/stripping cycles were completed at 10 mA cm^{-2}, and the *in situ* images are displayed in Fig. 16(c)–(j). No imaging was performed in the first half of either plating half cycle, then images were taken every minute. Before beam exposure, the Li deposit consisted of only one grain and exhibited a smooth overpotential profile. After beam exposure, the overpotential dropped and depicted much more noise. Near the end of the plating half cycle, more nucleation sites are evident along with the formation of a needle. After the initiation of the stripping half cycle, some Li is stripped away, however the half cycle only lasted 166 s before reaching the cutoff voltage indicating a low CE and dead Li is evident in Fig. 16(f). During the second cycle, the electrode was exposed to the electron beam for the entirety of the cycle, resulting in needle-like growth as well as the nucleation of new circular grains. The following stripping half cycle also resulted in low CE and the formation of dead Li.

The next observations were made with constant beam exposure during three full cycles at 10 mA cm^{-2}. The deposited Li during the first cycle resembled a bundle of balloons growing from the surface of the working electrode and after stripping a large amount of dead Li was evident resulting in new growth in the following two cycles. The current density applied in this experiment was the same as that of the experiment depicted in Fig. 16, yet the morphology of the deposited Li was vastly different, leading the group to the conclusion that the exposure of the Li surface to the electron beam resulted in a different SEI composition due to the reduction of radical species in the electrolyte. To visualize the effects of beam exposure alone,

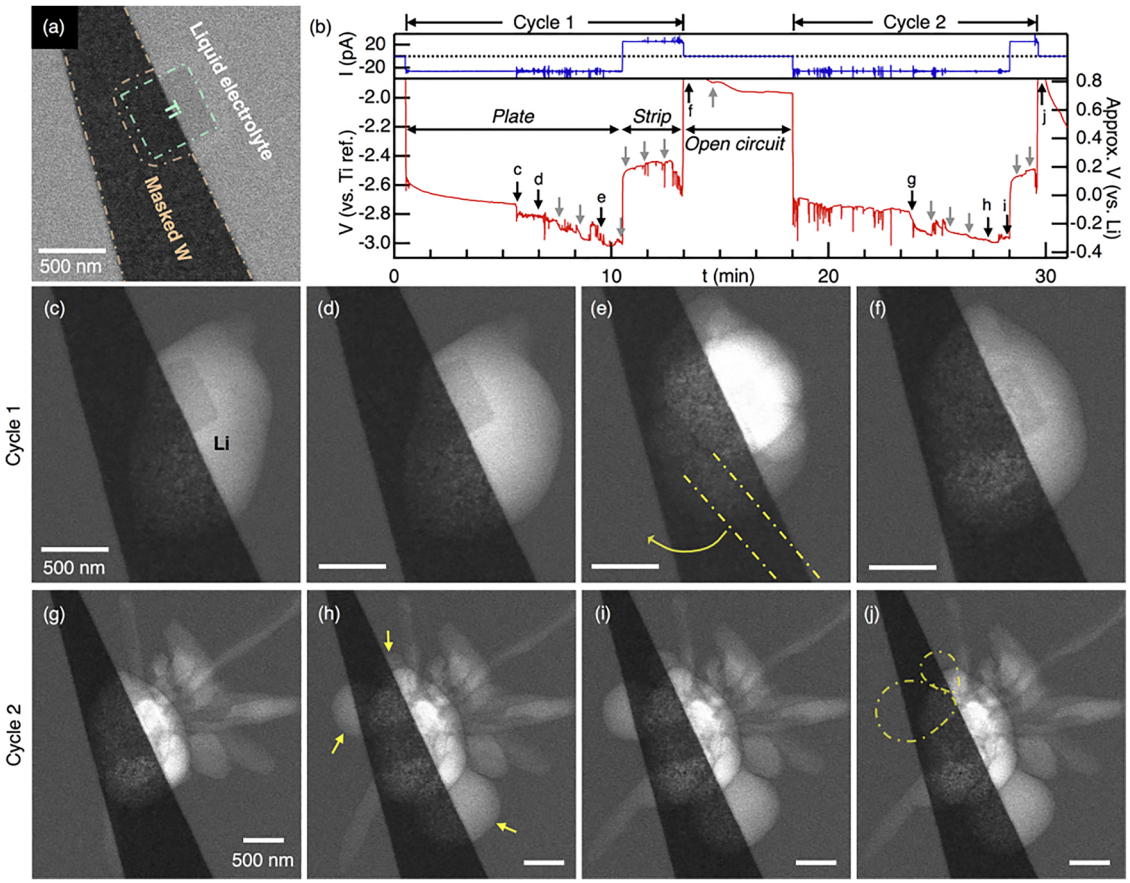

Fig. 16 (a) Bare electrode depicting Al_2O_3 masked tungsten and bare tungsten where deposition takes place. (b) Overpotential (*vs.* a large quasi-reference Ti electrode) and current profiles of two full cycles over time, with indicators depicting when images (c)–(j) were taken. (c)–(j) *In situ* TEM images of the Li deposition and dissolution over two full cycles. Reprinted (adapted) with permission from ref. 44. Copyright (2015) American Chemical Society.

the group plated Li onto a working electrode at less than 1 mA cm^{-2} while actively imaging the deposition. After 5 min of deposition and beam exposure, a dark region was evident around the deposited Li and remained after the Li was stripped away. Small areas of 75 nm^2 inside and away from the dark SEI area were then bombarded with the electron beam. The two areas inside the SEI exhibited a change in shade, becoming brighter than the surrounding area, while the area outside of the SEI did not change. Because the area inside the darker SEI became less dense than the electrolyte after electron beam bombardment, the group believes that this SEI is made of components like LiF that revert to metallic Li after beam exposure.

To further investigate the effects of beam exposure on Li deposition morphology, the group began cycling at 10 mA cm^{-2} on an unused Ti electrode. They completed one full cycle before imaging, so the morphology of the initially deposited Li could not be determined; however, the overpotential profile was smooth and the stripping achieved about a 90% CE. After this first cycle, images taken midway through the plating step of both the second and third cycles revealed faceted grains and needles. During stripping in the second cycle, dissolution started at a single point on the largest spherical grain and propagated outward until the grain was fully removed. The dissolution likely initiated at a weak point in the SEI, which could have led to dead Li if the defect caused necking or isolated a section of deposited Li.

Finally, the group compared high (25 mA cm^{-2}) and low (1 mA cm^{-2}) current density cycling on different working electrodes with consistent imaging and therefore consistent beam exposure. At low current density, Li deposited in spherical grains and stripped with high CE, exhibiting a smooth overpotential profile. This indicates to the group that the beam exposure posed less of an effect on the SEI. However, at high current density, dendrites and needle-like deposition were evident in even the first cycle. The overpotentials were much higher and had more noise, and the CEs were much lower than those at low current density. The findings made in this study were specific to the *in situ* TEM setup in that they expose the effects of electron beam exposure to the working electrode during deposition and dissolution. However, it also highlights the impact of SEI composition on Li deposition mechanisms. This study should be used to further understand and improve upon future *in situ* TEM studies on Li plating and stripping mechanisms.

A similar study by Mehdi *et al.* utilized an *in situ* visualization stage for observing Li deposition and stripping *via* STEM

on platinum (Pt) electrodes.[45] An electric field simulation was conducted to confirm the architecture of the cell would allow for reasonable plating and stripping dynamics. To ensure that the beam does not affect the deposition and stripping process, the group limited the beam dose to less than or equal to 0.3 e^{-} $Å^{-2}$ s^{-1}. To distinguish Li from the Pt working electrode and the $LiPF_6$/propylene carbonate (PC) electrolyte, the group utilized bright field imaging where anything denser than the electrolyte will appear lighter in the images while anything less dense than the electrolyte will appear darker.

The group began their investigation with three Li deposition/dissolution cycles, as illustrated in Fig. 17. The dissolution process in the first cycle was not fully reversible as revealed by the existence of residual Li deposits still visible on the Pt surface after the end of the stripping cycle (Fig. 17(a)). In the second cycle (Fig. 17(b)), Li deposits are much more dendritic and grow much larger with many visible voids. And again, large leftover Li is visible after the end of the stripping process. While Li deposits are visible on the surface of the Pt electrode, Pt and Li also alloy, and this is evident in the growth and shrinkage of the Pt electrode during cycling as well as in the cracks that are seen in the final electrochemical cycle (Fig. 17(c)). The group also performed a similar experiment at extended cycling in which the SEI layer, Li protrusions underneath the SEI layer, and the change in Pt electrode shape are clearly evident as are pockets of Li metal inside the Pt electrode. To obtain and analyze quantitative information from the *in situ* TEM observations, the group used a tracking algorithm to quantify the volume of Li metal deposited onto the Pt electrode seen in Fig. 17(a)–(c). Fig. 17(d)–(f) depict this quantification (Fig. 17(e)) as well as the CV (Fig. 17(d)) and SEI thickness growth (Fig. 17(f)) for the three cycles depicted in Fig. 17(a)–(c). They noted the difference between the volume of deposited Li in the second and third cycle *versus* the volume deposited in the first cycle is quite large. This is because, during the first cycle, Li is deposited relatively uniformly onto a smooth Pt electrode surface. After stripping, however, the surface is left rough and nonuniform due to a nonhomogeneous SEI and dead Li left behind. Therefore, the second and third plating processes are left to be conducted onto a surface with a nonuniform SEI layer with leftover dead Li leading to more dendritic morphology and even less reversibility. Consequently, Mehdi *et al.* collected qualitative information regarding the plating and stripping process of Li metal onto a Pt electrode with the *in situ* TEM. Implementing a tracking algorithm to quantify the materials in the *in situ* images, in particular, the group was able to show quantitative proof of their *in situ* cell.

Among other efforts, Kushima *et al.* used *in situ* ETEM to visualize Li deposition and model the mechanism for Li dendrite propagation and dissolution, creating dead Li and Li containing compounds or empty SEI shells.[46] They observed Li deposition onto a gold electrode through 1 M LiTFSI in dimethyl sulfoxide (DMSO) electrolyte. These observations allowed the group to model the development of Li dendrites through 4 stages: (1) a spherical dendrite nucleates at the surface and its diameter grows proportional to the square root of the time, (2) the dendrite grows from its root pushing the spherical nucleus away from the surface, (3) growth rate decreases significantly, perhaps due to the development of the SEI on the new growth, and (4) new, high growth rate begins again forming a kink and restarting the process.

Hou *et al.* conducted an *operando* study on the development of the SEI layer on gold (Au) anodes using mass-sensitive STEM.[47] Au was chosen as the anode material due to its alloying behavior with Li ions leading to large volume change upon lithiation and delithiation, replicating the volume change

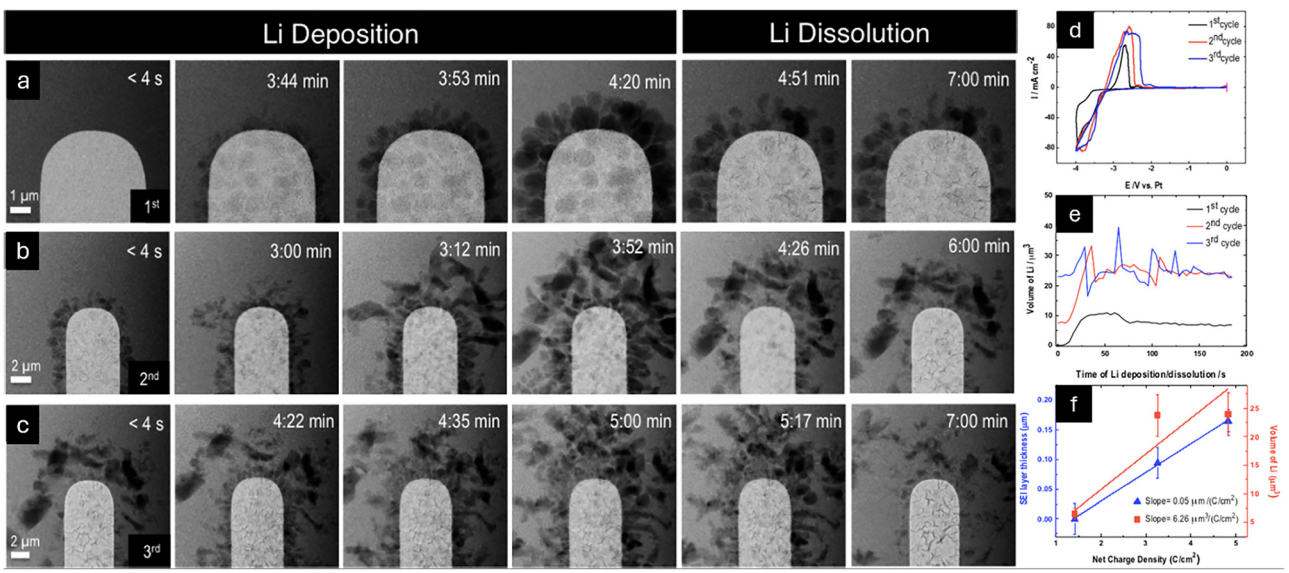

Fig. 17 *In situ* TEM images of Li deposition and dissolution: (a) first cycle, (b) second cycle, and (c) third cycle. (d) Cyclic voltammograms, (e) volume of deposited Li per cubic micron per cycle, and (f) SEI layer thickness and volume of deposited Li per net charge density of the *in situ* TEM experiment depicted in (a)–(c). Reprinted (adapted) with permission from ref. 45. Copyright (2015) American Chemical Society.

of a Li metal anode during charge and discharge and therefore replicating the parameters surrounding the formation of the SEI layer in a practical LMB. High-angle annular dark-field (HAADF) STEM was utilized to visualize the development of the SEI during Au lithiation due to the high mass-contrast revealing the SEI layer (Fig. 18(a)–(l)).

These *operando* observations show an uneven SEI thickness early in the lithiation cycle that eventually grows more even and thicker over time. The alloying process occurs more quickly in areas with a thin SEI layer, and spreads parallel to the Au/SEI interface (Fig. 18(d)), until most or all the interface has begun alloying, at which point the alloying layer grows in thickness (Fig. 18(g)–(l)). Because the Li–Au alloy grows quicker behind areas with a thinner SEI layer, the SEI layer is believed to suppress the diffusion of Li ions from the electrolyte to the electrode. To further investigate the formation of the SEI layer, the group analyzed and zoomed in on images of the SEI layer in the first 64 s of plating (Fig. 18(m)–(p)). The SEI film exposed due to higher magnification shows a typical inner layer consisting of inorganic compounds and a more porous outer layer of organic compounds closer to the electrolyte. Based on these observations, the group proposes a two-step process by which the SEI layer forms: (1) electrolyte decomposition occurs at the gold surface and thereby forms a thin, porous layer of both organic and inorganic compounds, then (2) electrolyte permeates into the layer and continuously decomposes over time, leaving an inorganic layer closer to the surface and an organic layer closer to the bulk electrolyte. The group also finds that the organic layer stops growing once the inner layer has become sufficiently dense, preventing further electrolyte decomposition. EELS spectra were taken of the two layers of the SEI, exposing the composition of the inorganic, inner SEI layer

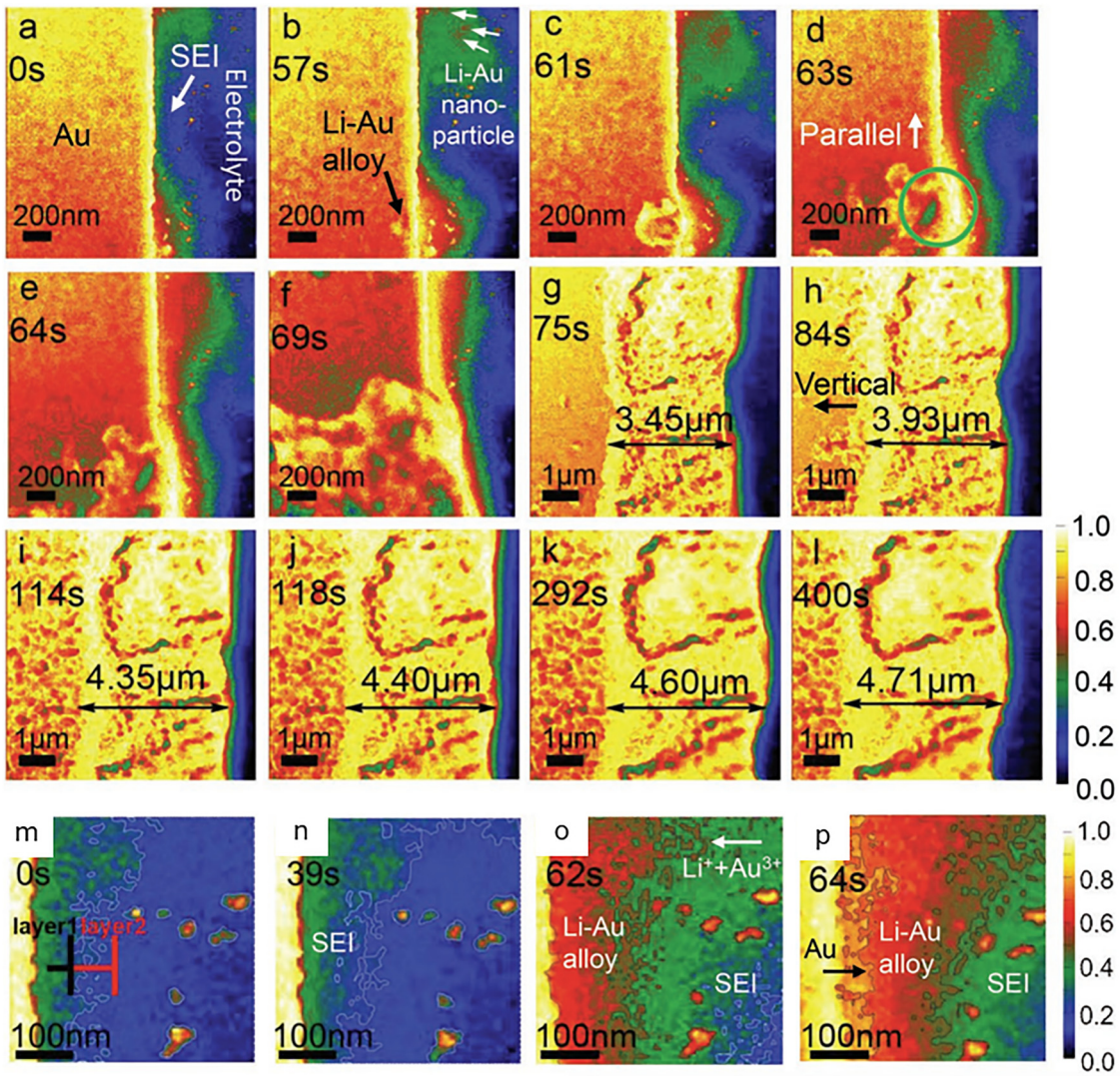

Fig. 18 HAADF STEM images of Au electrode lithiation, with time indications after beginning galvanostatic charging (a)–(l). High magnification HAADF STEM images of SEI development on the Au electrode in the first 64 s of lithiation (m)–(p). Electrolyte is dark/black, SEI film is green with blue consisting of a conglomeration of neutral and radical species produced by the initial electrolyte reduction, and the red/yellow areas are representative of the Au electrode with some red/yellow specks being Au–Li alloys. Reprinted (adapted) with permission from ref. 47. Copyright (2019) Wiley John and Sons.

consisting of Li compounds including dominantly Li carbonate and also LiF, LiOH and metallic Li. Another observation was conducted during the delithiation of the Au electrode exposing the failure mechanism of the SEI film where the film swells due to the shrinking of the Au electrode. As the electrode shrinks, the SEI roughens and dissolves into the electrolyte leading to exposure of the Au to the electrolyte directly, leading to rapid delithiation of the alloyed phase. The group concludes with cumulating their evidence to propose that SEI growth occurs at the SEI/electrolyte interface with the further reduction of the electrolyte. HAADF-STEM and ABF-STEM (not discussed here) allowed the group to distinguish between the inner and outer layers of the SEI and propose a formation and growth mechanism with these observations.

Ye *et al.* synthesized nitrogen-doped hollow porous carbon spheres (N-HPCS) as a possible nanostructure for housing Li deposition as an anode.[48] After synthesis and confirmation characterization with TEM, energy dispersive X-ray spectroscopy (EDX), X-ray photoelectron spectroscopy (XPS), and others, the group examined the nanostructures' validity as a possible solution to the challenges with Li metal, including dendritic deposition, SEI, and dead Li formation. To do this, the group utilized a dry cell configuration, touching a Li metal counter electrode with a Li_2O native layer employed as the solid electrolyte to the working electrode consisting of their N-HPCSs. An overpotential of −3 V was applied and the lithiation process was observed *via in situ* TEM analysis. The first step of lithiation observed was the thickening of the outer carbon shell and the widening of the inner hollow portion. This is evidence of Li filling the outer shell before plating inside the N-HPCS where crystalline Li fills the inner cavity with the resemblance of liquid filling a spherical container. Upon stripping, the overpotential is then reversed to +3 V and Li effectively drains out of the N-HPCS back to the counter electrode until it is fully delithiated. Then, the nanostructure returns to its empty size. After visualizing one full electrochemical cycle, the group observed similar plating and stripping for up to 50 cycles, observing no dendritic morphology and full lithiation and delithiation of several nanostructures. The group also noticed that lithiation did not immediately begin with the N-HPCS close to the Li source, but Li preferentially plated at seemingly random N-HPCSs. When one nanostructure is fully lithiated, the lithiation then moves on to the next nanostructure. The group also observed the performance differences in similar carbon nanostructures, such as with less N doping and reduced pores. Both alternatives resulted in dendritic deposition and an entirely different mechanism for plating than the N-HPCS. Finally, the group confirmed the utility of these structures in a coin cell configuration after plating with *ex situ* SEM where they observed full lithiation without dendritic morphology and high cyclability up to 270 cycles with a CE up to 98.5%. The *in situ* TEM methods utilized by this group allowed for the detailed explanation for the mechanisms of lithiation and delithiation of their novel nanostructure that tackles the challenges involved in Li metal anode implementation.

Chen *et al.* developed a novel *in situ* TEM cell that they use to expose a relationship between the SEI composition and the morphology of Li deposition.[49] The cell used a nickel grid substrate for Li deposition and an equimolar mixture of lithium bis(trifluoromethanesulfonyl)imide (LiTFSA) and tetraethylene glycol dimethyl ether (TEGDME) as the electrolyte with a counter electrode of $LiCoO_2$. The group imaged the substrate surface after applying a constant voltage of −4.25 V (*vs.* $LiCoO_2$) for 1 h and observed three different deposition morphologies described as fiber, moss, and film. Each of the growth modes observed are encapsulated by a thin shell (10–30 nm) that is believed to be the SEI. Using selected area electron diffraction (SAED), the group identified single crystalline Li metal with a body-centered cubic structure on a deposited Li fiber. The group also identified LiF from the LiTFSA electrolyte. Another SAED investigation of uniformly deposited Li revealed both LiF and Li_3N. Based on these findings, the group suggests that inorganic compounds like LiF and Li_3N support the desirable film-like Li deposition and suppress dendrite growth. With this *in situ* TEM visualization technique, the group observed three growth modes of Li deposition and identified a unique SEI composition on the most desirable growth mode, *i.e.*, 2D film-like deposition.

In another study, Sun *et al.* utilized two *in situ* TEM setups to observe Li plating and stripping through LLZTO SSE.[50] Both of these setups include a tungsten (W) substrate with a Li working electrode touching a chip of LLZTO solid electrolyte, which is held against the Li working electrode by either a Cu counter electrode or an AFM tip, which is used to investigate the growth of a Li dendrite underneath the solid electrolyte. Experimentation began with two full cycles of discharging and charging at approximately 4 mA cm^{-2} through the SSE using the Cu counter electrode setup. The first discharge half cycle yielded a cylindrical Li dendrite protruding from the top of the SSE (between the contact points of the Cu counter electrode), after discharge, a crumpled shell of the dendrite was left over, identified to be composed of Li_2CO_3. The following cycle resulted in new dendrite nucleation and following stripping resulted in a similar shell left over. The next experiments were conducted on the AFM tip setup, in which more dendrites nucleated below the SSE in the first discharge cycle, and similarly left behind a shell of Li_2CO_3 upon charging. The following cycles yielded dendrite nucleation above and below the SSE, also leaving behind the SEI or dead Li shell. Based on these results, the group concludes that Li prefers to deposit through fresh LLZTO without the Li_2CO_3 left behind because the fresh SSE has a Li^+ ion conductivity 4 times greater than Li_2CO_3. The group investigated the stripping dynamics of several dendrites that had grown from the bottom of the LLZTO chip in the AFM setup where they found that stripping can originate from the base, tip, and from the side of the dendrite and propagate toward the rest of the dendrite, removing all Li and leaving behind the Li_2CO_3 shell. The results of the experiments described in this study reveal the mechanisms of Li nucleation, growth, dendrite propagation, as well as the stripping mechanism where a shell of Li_2CO_3 is left behind. These

results are accumulated in a model proposed by the group in which particulates deposited inside the solid electrolyte swell until they bulge from the electrolyte eventually bursting upward in a columnar shape. Upon dissolution, the Li_2CO_3 shell is left.

Additionally, Gong *et al.* utilized *operando* TEM to expose the difference in Li plating and stripping mechanisms through LiF-rich and LiF-poor SEI layers.[51] The electrolytes used to promote these two different SEI layers were 1 M $LiPF_6$ in 1 : 1 EC : DMC with and without 5 wt% FEC. Cyclic voltammetry was conducted on the Pt electrodes submerged in the two electrolytes while STEM imaging was carried out at a beam exposure dose lower than the threshold needed for damage to occur. In the electrolyte without FEC, Li was deposited and grew into granular structures. The deposition mainly occurred at the ends of the 'dendrites' supposedly due to the change in electric field. After stripping, some dead Li was left behind. In the FEC added electrolyte, a similar morphology was evident, and dead Li was also left after stripping. A difference in the two experiments, however, was the formation of a bubble in the FEC added electrolyte as well as the evidence of an organic layer on the outer edges of the SEI. In the second cycle, however, the Li deposition in FEC-free electrolyte resulted in needle-like growth and after stripping resulted in dead Li. While the FEC-added study showed more uniform growth with much less dead Li produced after the stripping process. Through plasma focused ion beam – secondary ion mass spectroscopy (PFIB-SIMS) and nuclear magnetic resonance (NMR), the group confirmed the existence of more LiF in the SEI of the electrolyte with FEC added and later confirmed this SEI could suppress the formation of dead Li after 10 cycles.

Furthermore, Dachraoui *et al.* conducted a comprehensive study on the mechanisms involved in Li plating and stripping to and from a glassy carbon (GC) working electrode in 1 M $LiPF_6$ EC : EMC (3 : 7 by volume) electrolyte with 10 mmol L^{-1} ferrocene.[24] The group used a nanoscale *in situ* cell for STEM observations. Cyclic voltammetry was performed on the cell sweeping from 0 to −4 V at 20 mV s^{-1} and back to zero again, revealing two peaks. The first peak at −2 V corresponds to decomposition of the electrolyte, forming an SEI layer on the surface of the GC working electrode, and the second at −4 V is due to plating (and stripping in the reverse sweep) of Li ions on the working electrode. Fig. 19(a) depicts the observations made during the forward sweep from 0 V to −4 V at 20 mV s^{-1}. The first observation is made at 150 s depicting the reduction of the

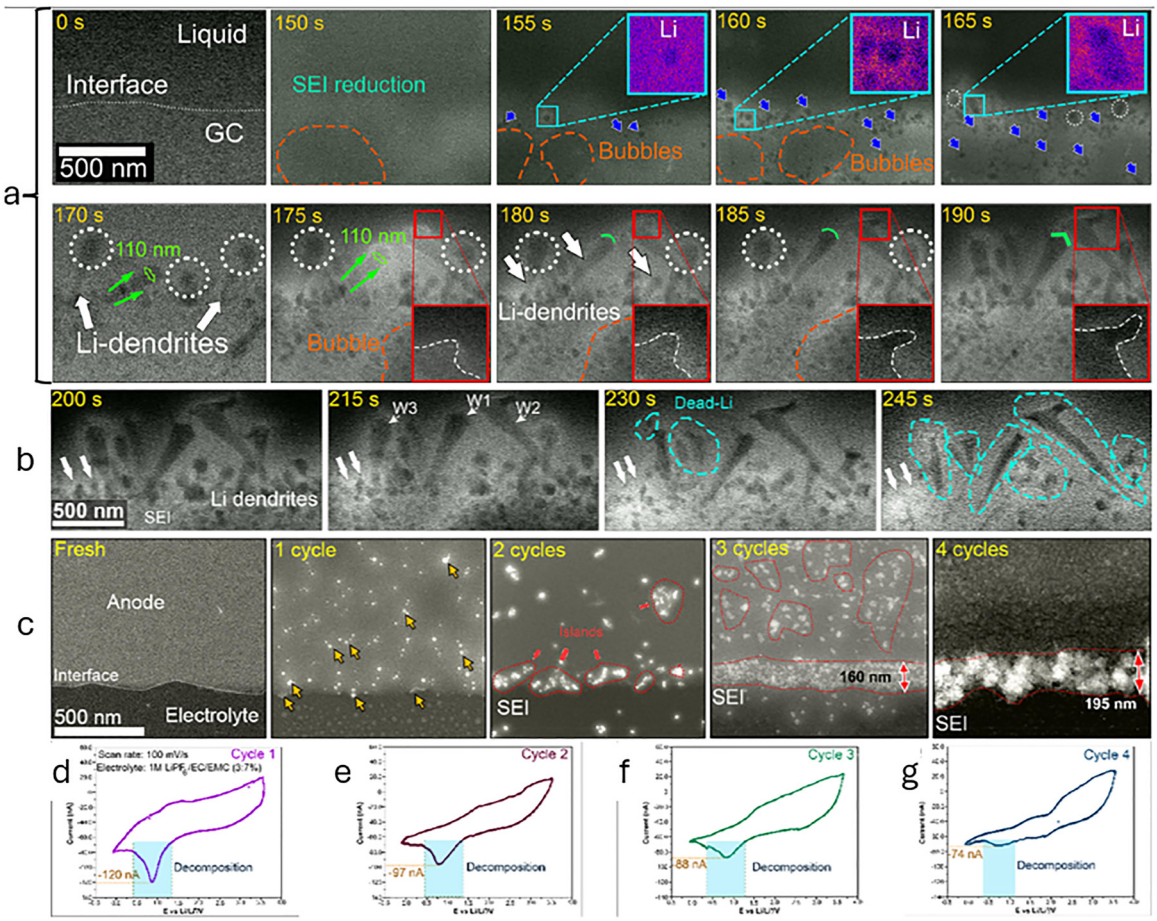

Fig. 19 (a) *In situ* S/TEM images recorded during the forward sweep depicting the formation of the SEI layer (150 s), deposition of Li nanoparticles under the SEI layer (155–165 s), and the growth of Li dendrites (170–190 s). (b) Dendrites formed as they are stripped in subsequent reverse CV sweep.[24] (c)–(g) SEI development over 4 cycles.[25] Reprinted (adapted) with permission from ref. 24 and 25 under a Creative Commons Attribution (CC BY) license.

SEI layer, made visible by the darkening of a region corresponding to a decrease in density in that region. Next, Li nanoparticles are visible under the SEI, and more and more nucleate until 170 s when dendrites begin to grow into the liquid electrolyte. The group explain this by contributing the switch from nanoparticle nucleation to dendrite growth to the breaking of the previously formed SEI layer due to tensile stress. After the initial SEI layer forms, it isolates the GC surface from the surrounding liquid electrolyte, preventing further SEI formation. As Li ions penetrate the SEI layer, they nucleate Li nanoparticles on the surface of the GC (as GC will not allow intercalation) underneath the SEI. As more of these Li NPs nucleate, they stretch the SEI layer, eventually cracking it, exposing Li to fresh electrolyte. This allows for Li ions to deposit directly onto the nanoparticles leading to tip growth – and therefore the growth of dendrites. As these dendrites grow, a new SEI layer forms on the surface of them, preventing further tip growth, therefore base growth pushes the dendrites away from the GC surface (170–185 s). As these dendrites continue to grow, they stretch and crack the new SEI allowing for more tip growth of dendrites creating branches (175–190 s). Fig. 19(b) depicts the images of the dendrites formed in Fig. 19(a) as they are stripped away in the following reverse CV sweep from −4 to 0 V. Stripping begins with the shrinking of the thickness of the dendrites, leading to isolation of the dendrites' tip because the base of these dendrites is thinner than the rest of the body. This stops further dissolution for some of the dendrites leading to dead Li, and for others the thin 'new' SEI allows for dissolution to occur around the surface of the dendrite, leading to some portions becoming isolated dead Li and for others to be completely stripped. These observations show that dissolution mechanisms vary from dendrite to dendrite, and that the mechanism itself is overly complex.

The observations made by Dachraoui *et al.* reveal the complexity of Li deposition and dissolution at the nanometer scale. These observations lead the group to formulate a model depicting the mechanisms of plating and stripping not described in this review. However, the model clearly depicts the observations and explanations described above. This paper strongly demonstrates the efficacy of *in situ* TEM experiments and their value in studying the electrochemical mechanisms of Li.

Another study by Dachraoi *et al.* utilized an *operando* electrochemical liquid cell for STEM to visualize the development of the SEI on a GC working electrode through continuously flowing 1 M $LiPF_6$ in EC:EMC electrolyte.[25] To observe the decomposition of the electrolyte, CV cycles in a range of 3.5 to −0.25 V (*vs.* Li/Li^+) were applied to the cell in succession. Fig. 19(c)–(g) depict the development of the SEI over 4 CV cycles at the aforementioned overpotential range and the corresponding CV curves. The first cycle (Fig. 19(d)) depicts a sharp peak at 0.75 V (*vs.* Li/Li^+) and high current, indicating a high rate of decomposition of the electrolyte. In the following cycles, the peak indicative of electrolyte decomposition lessens in current, indicating the layer of products of the decomposition is thickening and sealing portions of the GC working electrode from the electrolyte, preventing further decomposition. This can be confirmed in Fig. 19(c) with the layer of products thickening with each cycle, eventually sealing the electrode from the electrolyte. Using EDX on the SEI layer that had developed after 4 CV cycles, the group identified higher contents of carbon and oxygen in the outer region of the SEI layer while still seeing a distribution of fluorine, phosphorus, and silicon throughout the SEI. This evidence supports both models suggesting that inorganic products of electrolyte decomposition are more concentrated at or near the surface of the electrode, while more porous, inorganic products exist closer to the electrolyte, even though either may exist in the inner or outer portion of the electrolyte. The *operando* observations of SEI development made by Dachraoi *et al.* suggest the SEI is formed over the course of cycling in successive stages. The first stage is initiated by the decomposition of the $LiPF_6$ salt into inorganic compounds like LiF and their precipitation onto the surface of the electrode. Next, as more electrolyte decomposes, islands of these products form, and grow further as more electrolyte is consumed, eventually forming a layer. As cycling continues, decomposition continues with the production of more inorganic and organic products until the SEI is dense and covers the surface of the electrode.

All the afore-discussed investigations utilized *in situ* or *operando* TEM techniques to study the mechanisms of Li insertion or plating on various electrodes. Because these studies utilized novel or unique cells to house liquid electrolytes inside the high-vacuum TEM chambers, their findings can relate directly to the mechanisms of current and future LIB or LMB systems. Namely, Dachraoi *et al.*'s findings in the last two studies discussed show meaningful discussions of the Li plating mechanisms and the mechanisms of SEI formation at high magnification and in real time.

5. AFM observations on the evolution of Li dendrites

In situ AFM enables high resolution, real-time imaging of electrode surface topography during electrochemical cycling. Compared to electron-based techniques, AFM offers superior surface sensitivity, especially in the vertical dimension.[13] Recent *in situ* AFM research advancements have extensively captured these nanoscale mechanisms, particularly to investigate the SEI formation and changing dendrite morphology under various conditions.[52]

To understand the SEI layer development, Lin *et al.* investigated Li metal anodes using *in situ* AFM.[53] Their experimentation began with a composition study of the surface of as-received Li metal foil, identifying the native layer on the surface as Li_2O, LiOH, and Li_2CO_3 using XPS. Since the Li metal was not exposed to air, they claimed that the surface film originated from unavoidable reactions during supplier processing. After soaking the Li metal in PC solvent for 18 h, more pronounced surface features were present, and the oxygen signal peaked at

these surface features. These findings suggest that ridges and grain boundaries on the Li metal surface induce localized electric field enhancements, accelerating electrolyte solvent decomposition. Using the *in situ* AFM setup depicted in Fig. 20(a), the group observed the development of the SEI layer for up to 12 h. A line scan was taken at 0.5, 2, 6, and 12 h after submersion and the results were compared for their heights (Fig. 20(b)–(f)). The high points in the scan grew taller while the low points remained essentially the same height, validating the group's previous theory that the ridges, peaks, or other surface features accelerate PC decomposition and SEI growth at those points. They further scratched a 20 × 20 μm square on the Li metal surface and thereby observed how surface features evolved during submersion in the PC solvent for up to 72 h. The scratched surface quickly grew an SEI layer over the course of the submersion period, leading to significantly increased surface roughness across the entire scratched area. This was the opposite from the untouched Li surface which resulted in SEI developing primarily over the surface features such as ridges and grain boundaries. Given the results received with bare Li, Lin *et al.* further studied the protection effects of a nanoscale Al_2O_3 coating on Li metal. They deposited 100-cycle Al_2O_3 *via* atomic layer deposition (ALD) over Li metal. Using the *in situ* AFM setup, they observed the surface of the ALD-Al_2O_3-coated Li metal after submersion in the PC electrolyte for 0.5, 3, 6, and 12 h, as shown in Fig. 20(j)–(m). The roughness of the ALD protected Li surface increased at a much slower rate than the bare Li metal, as illustrated in Fig. 20(g). This demonstrated that the Al_2O_3 coating protected the Li metal and the PC from degradation. Also, the even distribution of oxygen signal across the surface after 24 h of submersion in the solvent further verified the prevention of decomposition at surface features. SEM imaging (Fig. 20(h)) and EDX mapping (Fig. 20(i)) were both applied to the same location and further confirmed these findings. In addition, the group observed the production of gasses during submersion of bare Li and coated Li in DME/DOL

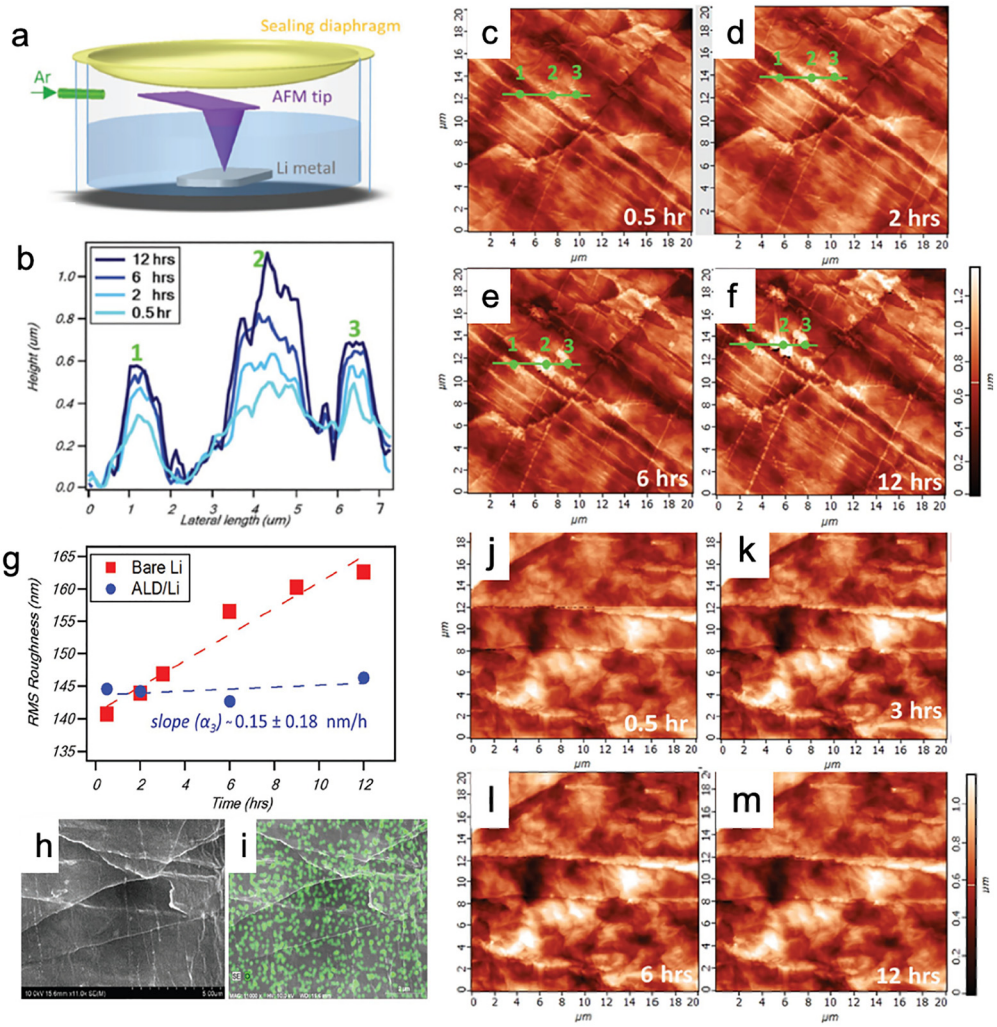

Fig. 20 (a) *In situ* AFM cell schematic. (b) Indication and comparison of line scans of *in situ* AFM images taken after (c) 0.5, (d) 2, (e) 6, and (f) 12 h of the Li surface soaked in PC solvent. (g) RMS roughness compared between bare and Al_2O_3 coated Li metal after submersion. (h) SEM and (i) EDX of the coated Li metal after 24 h of submersion in PC. *In situ* AFM images taken after (j) 0.5, (k) 3, (l) 6, and (m) 12 h of the coated Li surface submerged in PC solvent. Reprinted (adapted) with permission from ref. 53. Copyright (2016) Wiley John and Sons.

solvents (1/1) using an *in situ*/*operando* quadrupole mass spectrometer. Results showed a sharp production of CO, C_2H_4, and C_2H_5O with bare Li, while the ALD-coated Li produced no gasses during submersion and showed nearly the same gas production profile as that of DME/DOL without submerged Li. *In situ* AFM characterization also revealed that the bare Li surface evolved with time while the ALD-Al_2O_3 coating could protect the Li from decomposition.

Ultimately, AFM has provided excellent insight into the dynamic nature of the electrode surface and development of the SEI layer in Li-based batteries. The detailed vertical measurements allowed for 3D visualization of the SEI layer development in the form of surface roughness and SEI thickness. Combined with previous optical and electron-based techniques, AFM further encapsulates Li electrodeposition behaviors to provide a well-rounded analysis of its complex nature.

6. X-Ray microscopy studies on Li dendrites

In situ and *operando* X-ray microscopy techniques offer a powerful approach to visualize Li morphology evolution in real time under realistic operating conditions. The exceptional penetration capability of X-rays allow for the direct visualization of intact electrochemical cells, covering the entire hard X-ray ($> \sim 6$ keV) and soft X-ray ($< \sim 2$ keV) waveband.[54,55] Synchrotron radiation beams present high brightness and flux compared to lab-based X-rays, and are continuously adjustable by tuning the strength of bending magnets, insertion devices, and energy of the circulating electrons.[56]

Synchrotron X-ray imaging can be grouped into two categories based on their data acquisition strategy: full-field imaging methods and scanning imaging methods.[56,57] In a full-field microscope, the X-ray beam is focused down to a few micrometers, generating a large field of view to enable large images with fine resolution in a single shot without mechanical sample movements.[57] In contrast, scanning imaging methods focus the beam prior to illuminating the sample, performing a mechanical raster scan over the region of interest, acquiring images through individual pixels, then building up images point-by-point.[57] Thus, the spatial resolution is determined by a combination of beam and scanning step size. Full-field imaging offers higher image throughput, while scanning techniques allow for greater versatility in high contrast mechanisms.[57]

Of the two synchrotron X-ray imaging methods, the two prevalent techniques considered as microscopy are transmission X-ray microscopy (TXM), using full-field imaging, and scanning transmission X-ray microscopy (STXM), using scanning imaging. TXM provides high chemical sensitivity, high spatial resolution, environmental friendliness, and a thick penetration path.[58] It can be performed on thick samples in a real battery, such as a coin cell, with a large field of view in the micrometer range under an ambient pressure and atmosphere.[59,60] Cheng *et al.* was the first to utilize TXM for direct visualization of Li plating and stripping.[59] Inside a heat sealed plastic bag, a resin-insulated thin Cu wire was used as the working electrode and Li metal was deposited in $LiPF_6$ electrolyte, displayed in Fig. 21a. Performed at a constant current density of ~ 1 mA cm^{-2} for plating and stripping, images were taken periodically (Fig. 21b). In the corresponding

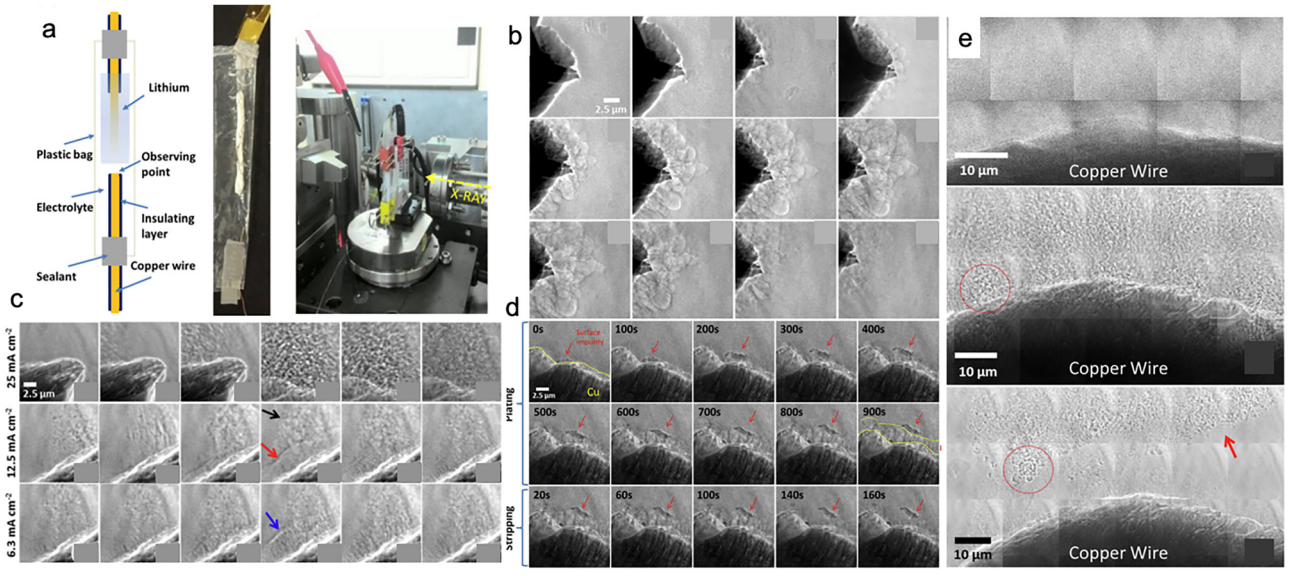

Fig. 21 (a) Cell setup using a heat sealed plastic bag and a resin-insulated thin Cu wire for the working electrode. (b) Plating and stripping performed at a constant current density of ~ 1 mA cm^{-2}, images were taken periodically. (c) Current density effects on dendritic evolution, plating/stripping at 25, 12.5, and 6.3 mA cm^{-2} in three subsequent cycles. (d) Plating and stripping with an SEI-isolated and electrochemically inactive dead Li impurity present, placed on the Cu electrode before cycling. (e) Mosaic images of a larger portion of the electrode surface. Reprinted (adapted) with permission from ref. 59. Copyright (2017) American Chemical Society.

images, the Cu is starkly contrasted as black compared to the electrolyte and semi-translucent Li deposits. The initial 680 s sees no Li deposition, as it was suggested the SEI layer formed during this period, though this is difficult to observe due to the thinness and atomic makeup similar to electrolyte. Li deposition is observed with nuclei continually growing and overlapping, developing a 5–7 μm thick deposit layer. The theoretical deposited Li layer at this current density is ~3.6 μm, indicating voids and pores are present within the mossy Li. Upon stripping, the Li layer shrinks and fades, leaving only a blurred layer with weak contrast, denoted as irreversible SEI or dead Li.

Fig. 21c demonstrates current density effects on dendrite formation, testing 25, 12.5, and 6.3 mA cm^{-2} in three subsequent plating/stripping cycles. The first cycle at a high current density created a porous, dendritic structure that grew quickly. The second and third cycles at lower current densities produced layers of Li with much smaller volume and higher CE, due to the more stable SEI formation and reduced irreversible Li deposits. The governing mechanism here is that Li-ion consumption on the surface, named 2-D growth, generally occurs at equal rates for all current densities. When the Li-ions near the surface are depleted, however, bulk solution ions are next to be reduced. As the metallic Li reduction is restrained by kinetic limitations, increased current density means quicker Li growth in height, named 3-D growth, meaning more rapid and porous branching dendrites. The black arrow in the figure points to the porous first cycle layer, while the red and blue arrows point to the higher density second and third cycle layers, respectively. Therefore, the growth type and porosity of Li is greatly influenced by current density during plating and stripping.

To further observe the effects of plating and stripping with an impurity present, an SEI-isolated and electrochemically inactive dead Li chunk was then placed on the Cu electrode before cycling (Fig. 20d). During plating, the impurity was lifted under the deposited Li layer, then remained in this position during the entirety of the stripping process. This result suggests dead Li will continually cause issues for further cycles, as it can agglomerate and cause an uneven Li surface, even when plating and stripping at lower current densities formed a denser and more uniform surface layer. To capture a larger portion of the electrode surface, Fig. 21e displays mosaic images, stitching several single images and eliminating the limitation of frame boundaries. The pristine Cu wire surface before cycling showed no evidence of impurities across the electrode. After one full cycle, a high-contrast layer is seen near the Cu surface, with a particularly contrasted region circled in red. In agreement with the *operando* images, this is dead Li that lost mechanical and electrochemical connection to the electrode. After the third cycle, there is a gap of low contrast between the electrode surface and the dead Li. It is suggested that continuous Li plating underneath this layer onto the electrode left a thin SEI isolation layer when stripped, simultaneously pushing the older dead Li away from the working electrode. The initial dead Li had a higher X-ray contrast than the residual SEI/dead Li structure that remained from subsequent cycles, creating a gap between the dead Li from the first cycle and the electrode. The X-ray microscopy images here illustrate the irreversible composition differences left behind from the first and remaining cycles, including why dead Li can be seen extending from the electrode with continued cycling. More extensive experiments will be necessary to determine the overall effects of dead Li on cycling using this method, though distinct details have been captured in this imaging.

This experiment demonstrates TXM as a unique technique to observe Li morphology evolution in *operando* conditions. It emphasized the effects of current density and repeated cycling on dead Li formation and SEI development, using the high spatial resolution and thick penetration properties of hard X-rays to their advantage. It is one of only a very few studies using *in situ* TXM, as the high equipment cost and complex reconstruction software both pose significant challenges in its wide implementation.[61] Cook *et al.* used TXM to image tin anodes at several points during cycling, while Olivares-Marín *et al.* observed cathode reactions in a Li–O_2 cell, both proving full-field X-ray imaging techniques to be a powerful characterization tool for different Li-based battery chemistries.[62,63] The main limitation of TXM is its poor image contrast for light elements due to the low X-ray absorption in the hard X-ray energy range.[59] More research attention should be focused on this technique as a viable way to better understand Li growth and morphology.

STXM is a scanning microscopy technique that reveals chemical heterogeneity and diffusion dynamics for better Li-ion transport observations, also capable of light-element identification.[56,58,64] Due to the required vacuum chamber, a specially designed cell is required to avoid liquid electrolyte evaporation, which can complicate *operando* experiments.[65] Additionally, the low penetration path under soft X-rays requires a thin sample, generally single-layer particles, and less electrolyte for optimal image quality.[65] There have been several experiments that use STXM to effectively visualize Li-ion behavior in *operando* conditions. Lim *et al.* used STXM to observe Li insertion into $LiFePO_4$ cathodes at single-particle resolution, revealing the key role in the heterogeneous Li surface reaction rate.[66] Li *et al.* combined TEM and STXM to image $LiFePO_4$ cathode lithiation, identifying crucial current density effects on cycling rates, exemplifying the ability to combine microscopy techniques effectively.[67] However, there are no published experiments to date that utilize STXM to purely observe LMA morphology under *in situ* or *operando* conditions.

X-ray fluorescence microscopy (XFM) and coherent diffractive imaging (CDI) are two intriguing X-ray techniques that may be used in future studies. XFM has recently been applied in sensitive element analysis, as it can map trace elements in a sample by analyzing emitted secondary photons. This form of spatial mapping is a notable method for both heterogenous or homogeneous structures, as its ability to combine with SEM or TXM can provide unique information.[68] However, its long acquisition time required to obtain a reasonable signal-to-noise ratio for each pixel is time-consuming and limits its *operando* application. CDI represents a lens-less form of X-ray microscopy that can theoretically reach atomic-scale resolutions

beyond the diffraction limit of optic based X-ray microscopes. Currently, a spatial resolution of ~10 nm has been achieved with coherent X-ray sources, reconstructed using the phase-retrieval algorithms from CDI.[58] Taking advantage of next-generation X-ray sources, CDI and XFM are expected to simultaneously achieve higher spatial and temporal resolution to expand the current understanding of electrochemical kinetics in battery reactions.

Projection-based imaging methods such as X-ray radiography and X-ray tomography (XRT) are not considered microscopy techniques but are crucial characterization methods for observing Li metal behavior. Synchrotron X-ray radiography, also referred to as X-ray imaging (XRI), is a 2-D imaging technique where the synchrotron X-rays transmitted through the sample are converted into visible light by a scintillator, then magnified and imaged with a camera using a detector or charge-coupled device.[69,70] It allows for real time visualization of dendrite formation, providing clear contrast of bulk Li and deposited Li on the surface. Jeoun *et al.* used *operando* XRI to observe Li plating behavior in a new electrolyte (1 M $LiPF_6$ in equal parts EC, DEC, EMC, and DME, termed the pentamery electrolyte (PenE)) (Fig. 22a).[69] Different from common 1 M $LiPF_6$ nucleation, Li deposition in PenE was observed in the images as dendrite-free with a dense layer of homogeneous thickness across the entire electrode (Fig. 22b and c), an important trait for reversibility in LMB applications. Yu *et al.* used XRI to observe plating and stripping under practical battery conditions, then to measure $CsPF_6$ additive effectiveness in suppressing dendrites to determine Li's complex mechanisms.[71] Using an *operando* technique in these cases were especially helpful, as the sharp dendrite edges turned into smoother surfaces, so *ex situ* images could appear similar to the bulk Li surface.

From the set of over 1000 2-D radiographic images that can be taken at various angles on an axis perpendicular to the incident beam, 3-D images can be generated to form a reconstructed internal sample structure.[72] This process is known as tomography, which uses software to combine the images and encompass the entire volume imaged into a single diagram. XRT can accurately distinguish bulk Li from the electrochemically generated high specific surface area Li, the accuracy of which is determined by the spatial resolution of the radiographic measurement and the reconstruction software.[54,56] The high resolution and extensible versatility of XRI and XRT enables both 2-D and 3-D visualizations of the internal processes, making these synchrotron-based imaging methods powerful tools for battery research. Harry *et al.* carried out the first experiment to image Li growth using 2-D X-ray tomography slices and reconstruct them into 3-D volumes, capturing the symmetric Li metal cell after various amounts of charge passed during cycling.[73] The *operando* 2-D images (Fig. 22d)

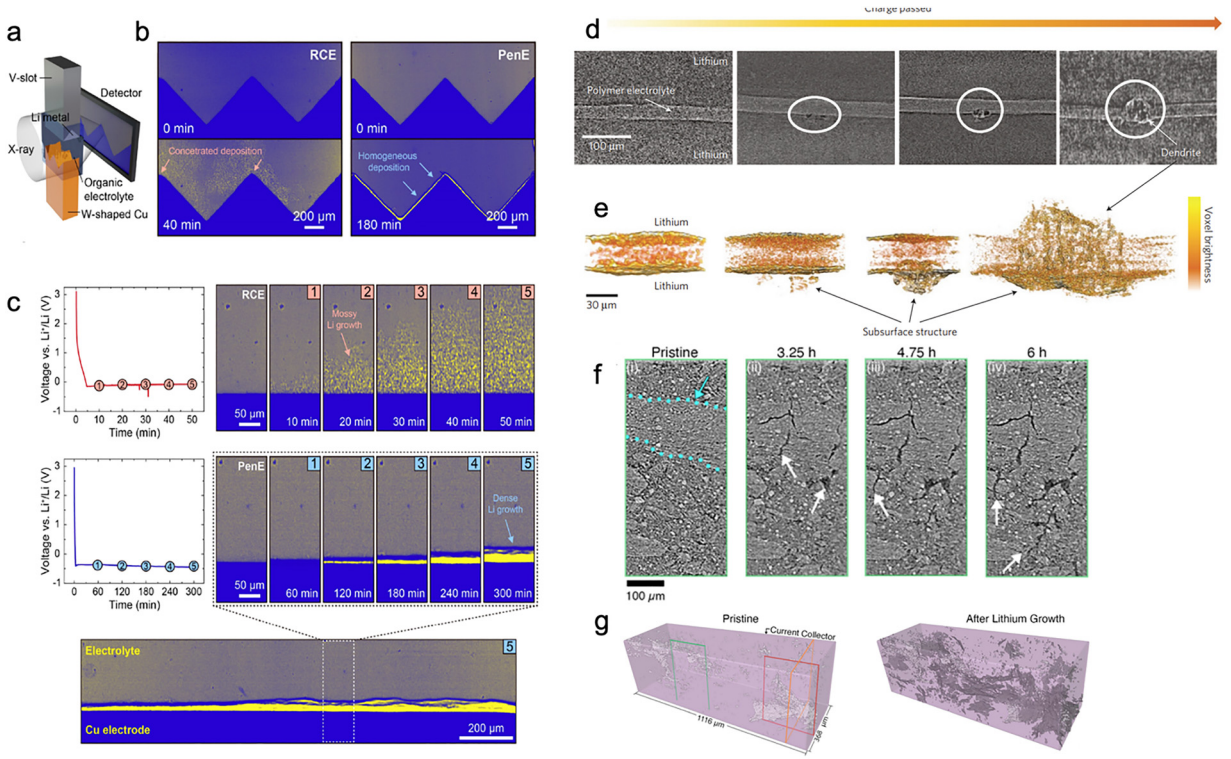

Fig. 22 (a) and (b) Cell setup and *operando* XRI images to observe Li plating behavior in PenE electrolyte.[69] (c) XRI observing plating in both the reference electrolyte and with a $CsPF_6$ additive. (d) *Operando* 2-D radiography images and (e) their 3-D reconstructions capture the LMA's transition from clear electrode/electrolyte interfaces to large and clearly visible heterogeneity across both electrodes.[73] (f) *Operando* 2-D radiographs and (g) reconstructed 3-D imaging within a cell, highlighting crack evolution during Li filament growth.[74] Reprinted (adapted) with permission from ref. 69. Copyright (2022) American Chemical Society. Reprinted (adapted) with permission from ref. 73. Copyright (2013) Springer Nature.

capture the LMA's transition during cycling from clear electrode/electrolyte interfaces to large and clearly visible dendrites across both electrodes when the cell shorts. The 3-D reconstructions (Fig. 22e) provide an in depth look into the damaging dendritic growth, capturing an interestingly split between the electrode and electrolyte, both containing Li and polymer separator material. Sandoval *et al.* used X-ray computed tomography to observe and analyze Li behavior in SSEs at varying resistance, including *operando* 2-D (Fig. 22f) and reconstructed 3-D imaging (Fig. 22g) within the cell.[74] The 3-D reconstruction enabled filament-driven crack analyzation to better understand SSE particle size on Li-ion resistance and porosity, including how existing cracks evolve during plating and its subsequent stripping. Thus, *operando* 2-D and 3-D XRT provides substantial information regarding microstructural changes including volume change, feature size, specific area, and curvature distribution, as well as chemical evolution during battery cycling.

Overall, there has been very few studies conducting *in situ* or *operando* X-ray microscopy using a synchrotron, as both the high equipment cost and complex reconstruction software pose significant challenges in their wide implementation on LMAs. X-ray microscopies have proven to allow for more realistic experimental setups, but have a limited resolution based on beam and scanning step size.[56] There will likely be an increased usage of this technique in the future, as it provides several unique benefits not available with other microscopy techniques. The resolution range of X-ray microscopy lies between OM and electron microscopies, while the contrast of synchrotron-based X-ray absorption reveals important morphological details such as solidity and porosity.[75] Its nonvacuum condition can be considered a distinct advantage to provide information on the internal structure of the materials while in realistic conditions.[75] One concern is possible radiation damage to samples, which may occur during *operando* battery experiments with liquid electrolytes that are more sensitive to a synchrotron X-ray beam.[58] In order to allow X-rays to penetrate the cell to perform in *operando* synchrotron X-ray characterization, modifications to the coin cell typically involve perforation of the X-ray attenuating, a conductive stainless-steel casing, and then sealing with an X-ray transparent thin film.[58] Nevertheless, *operando* X-ray microscopy techniques can be used as a powerful, non-destructive approach to visualizing Li morphology evolution in a realistic cell setup.

7. Conclusion and outlook

A comprehensive understanding of LMA behavior remains fundamental to realizing high-energy-density rechargeable batteries. Despite significant progress, the complex relationships of electrochemical, mechanical, and chemical processes that govern Li deposition and dissolution continues to challenge the stability and reversibility of LMAs. Through recent imaging advancements, researchers have gradually uncovered the dynamic evolution of dendrites, the formation and reactions of an SEI, and the pathways allowing short-circuit failure with novel clarity.

The center of these advances is the emergence of *in situ* and *operando* microscopy, transforming how Li interfacial behavior can be studied. *In situ* microscopy enables direct observations of structural and morphological evolution under carefully controlled environments, linking Li morphology with voltage response, current distribution, and CE. *Operando* microscopy extends this capability through synchronized imaging with realistic operating conditions, providing valuable mechanical insights into nucleation, SEI growth, and void formation. These temporal advantages have enabled visualization of morphological evolution while simultaneously tracking electrochemical processes, a feature not possible with *ex situ* measurements. The ability to observe Li metal phenomena under realistic conditions without removal from its environment further demonstrates *in situ* and *operando* importance, as their further integration into imaging systems will strengthen their role far beyond the existing *ex situ* techniques.

Among all microscopy techniques, OM remains an invaluable method for directly observing morphological transformations during cycling. It offers wide-field, real-time visualization of dendritic growth and surface evolution on the macroscopic scale, capturing the fundamental behaviors of Li deposition and dissolution. SEM provides much higher spatial resolution, revealing the fine structural features, nucleation patterns, and interfacial roughening under sub-micron precision. TEM delivers atomic-level insights into SEI composition, interfacial reactions, and crystal structure evolution unlike any other microscopy method. However, electron beam microscopies suffer from beam sensitivity, vacuum restraints, and functional cells that remain as demanding obstacles. AFM complements these techniques by quantifying nanoscale topography, tracking local surface evolution with exceptional sensitivity. More recently, X-ray microscopy has implemented both synchrotron-based and laboratory-scale methods to non-destructively probe internal structures and reconstruct 3-D morphologies. This new technique for observing Li behavior has combined its chemical sensitivity with deep penetration for a promising opportunity to correlate Li distribution and SEI heterogeneity across multiple scales. Collectively, these imaging modes can form versatile experimental parameters for investigating the physical and chemical mechanisms governing LMA degradation.

The greatest promise for future progress will be combining these techniques into a complementary framework. Strategies that can effectively integrate the wide-field temporal tracking of OM, the high-resolution surface imaging of electron microscopy, the mechanical and topographical quantification of AFM, and the volumetric chemical mapping of X-ray microscopy will enable a more well-rounded understanding of Li behavior and beyond. The range from the atomic to the macroscopic scale, combined with *in situ* and *operando* measurements, can provide extensive insight across several aspects of battery performance. A pressing challenge for this field is to translate these characterization setups from optimized laboratory environments to realistic conditions of practical batteries. Most studies to date have utilized simplified cells, using moderate current densities and excess electrolyte. These

parameters can achieve success in moderate configurations, but can diverge significantly from commercial-scale applications. *In situ* and *operando* microscopy must be adapted to formats essential for understanding Li mechanisms under realistic stresses, requiring innovation of cell designs, environmental control, and improved materials and interfaces compatible with realistic conditions.

As the field advances, *in situ* and *operando* microscopy will continue to redefine how Li metal interfaces are understood, bridging the divide between fundamental electrochemistry and practical battery operation. By enabling real-time visualization of Li evolution under realistic conditions, these approaches will not only clarify the mechanisms governing instability and failure, but also provide rational design insights of interfacial solutions that promote uniform deposition, efficient long-term cycling. Continued progress in cell engineering and imaging technologies will further improve these methods for increasingly practical and complex systems, more relevant for commercial applications. Ultimately, these advances will drive a more comprehensive, mechanistic understanding of Li metal behavior, guiding the development of safer and more reliable next-generation energy storage technologies.

Conflicts of interest

There are no conflicts to declare.

Data availability

This article is a review article. All data discussed are from previously published sources, which are cited in the manuscript.

Acknowledgements

This study was supported by the U. S. National Science Foundation with the award number OIA-2429581. X. M. also appreciates the support of Twenty-First Century Professorship from the University of Arkansas, Fayetteville, Arkansas, USA.

References

1 M. S. Whittingham, Electrical energy storage and intercalation chemistry, *Science*, 1976, **192**(4244), 1126–1127, DOI: 10.1126/science.192.4244.1126.
2 W. Xu, *et al.*, Lithium metal anodes for rechargeable batteries, *Energy Environ. Sci.*, 2014, **7**(2), 513–537, DOI: 10.1039/C3EE40795K.
3 K. Mizushima, P. C. Jones, P. J. Wiseman and J. B. Goodenough, Li_xCoO_2 ($0 < x < 1$): a new cathode material for batteries of high energy density, *Mater. Res. Bull.*, 1980, **15**(6), 783–789, DOI: 10.1016/0025-5408(80)90012-4.
4 R. Yazami and P. Touzain, A reversible graphite-lithium negative electrode for electrochemical generators, *J. Power Sources*, 1983, **9**(3), 365–371, DOI: 10.1016/0378-7753(83)87040-2.
5 A. Yoshino and T. Nakajima, *US Pat.*, 4668595, 1987.
6 R. K. Petla, I. Lindsey, J. Li and X. Meng, Interface modifications of lithium metal anode for lithium metal batteries, *ChemSusChem*, 2024, **17**(17), e202400281, DOI: 10.1002/cssc.202400281.
7 J. B. Goodenough and Y. Kim, Challenges for rechargeable Li batteries, *Chem. Mater.*, 2010, **22**(3), 587–603, DOI: 10.1021/cm901452z.
8 E. Peled, D. Golodnitsky and G. Ardel, Advanced model for solid electrolyte interphase electrodes in liquid and polymer electrolytes, *J. Electrochem. Soc.*, 1997, **144**(8), L208, DOI: 10.1149/1.1837858.
9 A. J. Sanchez, E. Kazyak, Y. Chen, K.-H. Chen, E. R. Pattison and N. P. Dasgupta, Plan-view operando video microscopy of Li metal anodes: identifying the coupled relationships among nucleation, morphology, and reversibility, *ACS Energy Lett.*, 2020, **5**(3), 994–1004, DOI: 10.1021/acsenergylett.0c00215.
10 X. Shen, *et al.*, The dynamic evolution of aggregated lithium dendrites in lithium metal batteries, *Chin. J. Chem. Eng.*, 2021, **37**, 137–143, DOI: 10.1016/j.cjche.2021.05.008.
11 B.-K. Cho, S.-Y. Jung, S.-J. Park, J.-H. Hyun and S.-H. Yu, *In Situ*/Operando Imaging Techniques for Next-Generation Battery Analysis, *ACS Energy Lett.*, 2024, **9**(8), 4068–4092, DOI: 10.1021/acsenergylett.4c01098.
12 M. Motoyama, In situ microscopy techniques for understanding Li plating and stripping in solid-state batteries, *Microscopy*, 2024, **73**(2), 184–195, DOI: 10.1093/jmicro/dfad058.
13 S. Lee, *et al.*, In situ techniques for Li-rechargeable battery analysis, *Carbon Energy*, 2024, **6**(12), e549, DOI: 10.1002/cey2.549.
14 K. N. Wood, *et al.*, Dendrites and Pits: Untangling the Complex Behavior of Lithium Metal Anodes through Operando Video Microscopy, *ACS Cent. Sci.*, 2016, **2**(11), 790–801, DOI: 10.1021/acscentsci.6b00260.
15 J. Steiger, D. Kramer and R. Mönig, Mechanisms of dendritic growth investigated by *in situ* light microscopy during electrodeposition and dissolution of lithium, *J. Power Sources*, 2014, **261**, 112–119, DOI: 10.1016/j.jpowsour.2014.03.029.
16 P. Bai, J. Li, F. R. Brushett and M. Z. Bazant, Transition of lithium growth mechanisms in liquid electrolytes, *Energy Environ. Sci.*, 2016, **9**(10), 3221–3229, DOI: 10.1039/C6EE01674J.
17 C.-J. Huang, *et al.*, The Entanglement of Li Capping and Deposition: An Operando Optical Microscopy Study, *ACS Nano*, 2023, **17**(14), 13241–13255, DOI: 10.1021/acsnano.3c00640.
18 K.-H. Chen, *et al.*, Dead lithium: mass transport effects on voltage, capacity, and failure of lithium metal anodes, *J. Mater. Chem. A*, 2017, **5**(23), 11671–11681, DOI: 10.1039/C7TA00371D.
19 L. Porz, *et al.*, Mechanism of Lithium Metal Penetration through Inorganic Solid Electrolytes, *Adv. Energy Mater.*, 2017, **7**(20), 1701003, DOI: 10.1002/aenm.201701003.
20 S. E. Sandoval, *et al.*, Understanding the Effects of Alloy Films on the Electrochemical Behavior of Lithium Metal

Anodes with Operando Optical Microscopy, *J. Electrochem. Soc.*, 2021, **168**(10), 100517, DOI: 10.1149/1945-7111/ac2d11.
21 W. Tang, *et al.*, Lithium Silicide Surface Enrichment: A Solution to Lithium Metal Battery, *Adv. Mater.*, 2018, **30**(34), 1801745, DOI: 10.1002/adma.201801745.
22 H. Zhang, S. Ju, G. Xia, D. Sun and X. Yu, Dendrite-Free Li-Metal Anode Enabled by Dendritic Structure, *Adv. Funct. Mater.*, 2021, **31**(16), 2009712, DOI: 10.1002/adfm.202009712.
23 X. Shi, *et al.*, Solid Electrolyte Interphase Recombination on Graphene Nanoribbons for Lithium Anode, *ACS Nano*, 2024, **18**(12), 8827–8838, DOI: 10.1021/acsnano.3c11796.
24 W. Dachraoui, R.-S. Kühnel, C. Battaglia and R. Erni, Nucleation, growth and dissolution of Li metal dendrites and the formation of dead Li in Li-ion batteries investigated by operando electrochemical liquid cell scanning transmission electron microscopy, *Nano Energy*, 2024, **130**, 110086, DOI: 10.1016/j.nanoen.2024.110086.
25 W. Dachraoui, R. Pauer, C. Battaglia and R. Erni, Operando electrochemical liquid cell scanning transmission electron microscopy investigation of the growth and evolution of the mosaic solid electrolyte interphase for lithium-ion batteries, *ACS Nano*, 2023, **17**(20), 20434–20444, DOI: 10.1021/acsnano.3c06879.
26 C. Cui, *et al.*, Unlocking the in situ Li plating dynamics and evolution mediated by diverse metallic substrates in all-solid-state batteries, *Sci. Adv.*, 2022, **8**(43), eadd2000, DOI: 10.1126/sciadv.add2000.
27 M. S. Leite, *et al.*, Insights into capacity loss mechanisms of all-solid-state Li-ion batteries with Al anodes, *J. Mater. Chem. A*, 2014, **2**(48), 20552–20559, DOI: 10.1039/C4TA03716B.
28 M. Golozar, *et al.*, In situ observation of solid electrolyte interphase evolution in a lithium metal battery, *Commun. Chem.*, 2019, **2**(1), 1–9, DOI: 10.1038/s42004-019-0234-0.
29 M. Golozar, *et al.*, In situ scanning electron microscopy detection of carbide nature of dendrites in Li–polymer batteries, *Nano Lett.*, 2018, **18**(12), 7583–7589, DOI: 10.1021/acs.nanolett.8b03148.
30 M. Nagao, A. Hayashi, M. Tatsumisago, T. Kanetsuku, T. Tsuda and S. Kuwabata, In situ SEM study of a lithium deposition and dissolution mechanism in a bulk-type solid-state cell with a Li2S–P2S5 solid electrolyte, *Phys. Chem. Chem. Phys.*, 2013, **15**(42), 18600, DOI: 10.1039/c3cp51059j.
31 J. Zhao, *et al.*, In situ observation of Li deposition-induced cracking in garnet solid electrolytes, *Energy Environ. Mater.*, 2022, **5**(2), 524–532, DOI: 10.1002/eem2.12261.
32 F. Sagane, R. Shimokawa, H. Sano, H. Sakaebe and Y. Iriyama, In situ scanning electron microscopy observations of Li plating and stripping reactions at the lithium phosphorus oxynitride glass electrolyte/Cu interface, *J. Power Sources*, 2013, **225**, 245–250, DOI: 10.1016/j.jpowsour.2012.10.026.
33 M. Motoyama, M. Ejiri and Y. Iriyama, In-Situ electron microscope observations of electrochemical Li deposition/dissolution with a LiPON electrolyte, *Electrochemistry*, 2014, **82**(5), 364–368, DOI: 10.5796/electrochemistry.82.364.
34 M. Motoyama, M. Ejiri, H. Nakajima and Y. Iriyama, Mechanical failure of Cu current collector films affecting Li plating/stripping cycles at Cu/LiPON interfaces, *J. Electrochem. Soc.*, 2023, **170**(1), 012503, DOI: 10.1149/1945-7111/aca79d.
35 M. Motoyama, M. Ejiri, T. Yamamoto and Y. Iriyama, *In situ* scanning electron microscope observations of Li plating/stripping reactions with Pt current collectors on LiPON electrolyte, *J. Electrochem. Soc.*, 2018, **165**(7), A1338–A1347, DOI: 10.1149/2.0411807jes.
36 A. Yulaev, *et al.*, From microparticles to nanowires and back: radical transformations in plated Li metal morphology revealed via *in situ* scanning electron microscopy, *Nano Lett.*, 2018, **18**(3), 1644–1650, DOI: 10.1021/acs.nanolett.7b04518.
37 M. Motoyama, Y. Tanaka, T. Yamamoto, N. Tsuchimine, S. Kobayashi and Y. Iriyama, The active interface of Ta-doped $Li_7La_3Zr_2O_{12}$ for Li plating/stripping revealed by acid aqueous etching, *ACS Appl. Energy Mater.*, 2019, **2**(9), 6720–6731, DOI: 10.1021/acsaem.9b01193.
38 L. Zhang, *et al.*, Lithium whisker growth and stress generation in an in situ atomic force microscope–environmental transmission electron microscope set-up, *Nat. Nanotechnol.*, 2020, **15**(2), 94–98, DOI: 10.1038/s41565-019-0604-x.
39 T. Krauskopf, *et al.*, Lithium-metal growth kinetics on LLZO garnet-type solid electrolytes, *Joule*, 2019, **3**(8), 2030–2049, DOI: 10.1016/j.joule.2019.06.013.
40 X. Xie, J. Xing, D. Hu, H. Gu, C. Chen and X. Guo, Lithium expulsion from the solid-state electrolyte $Li_{6.4}La_3Zr_{1.4}Ta_{0.6}O_{12}$ by controlled electron injection in a SEM, *ACS Appl. Mater. Interfaces*, 2018, **10**(6), 5978–5983, DOI: 10.1021/acsami.7b17276.
41 T. Krauskopf, B. Mogwitz, H. Hartmann, D. K. Singh, W. G. Zeier and J. Janek, The fast charge transfer kinetics of the lithium metal anode on the garnet-type solid electrolyte $Li_{6.25}Al_{0.25}La_3Zr_2O_{12}$, *Adv. Energy Mater.*, 2020, **10**(27), 2000945, DOI: 10.1002/aenm.202000945.
42 Y. Liu, *et al.*, Lithiation-induced embrittlement of multi-walled carbon nanotubes, *ACS Nano*, 2011, **5**(9), 7245–7253, DOI: 10.1021/nn202071y.
43 X. Lu, T. D. Bogart, M. Gu, C. Wang and B. A. Korgel, In situ TEM observations of Sn-containing silicon nanowires undergoing reversible pore formation due to fast lithiation/delithiation kinetics, *J. Phys. Chem. C*, 2015, **119**(38), 21889–21895, DOI: 10.1021/acs.jpcc.5b06386.
44 A. J. Leenheer, K. L. Jungjohann, K. R. Zavadil, J. P. Sullivan and C. T. Harris, Lithium Electrodeposition Dynamics in Aprotic Electrolyte Observed in Situ via Transmission Electron Microscopy, *ACS Nano*, 2015, **9**(4), 4379–4389, DOI: 10.1021/acsnano.5b00876.
45 B. L. Mehdi, *et al.*, Observation and quantification of nanoscale processes in lithium batteries by operando electrochemical (S)TEM, *Nano Lett.*, 2015, **15**(3), 2168–2173, DOI: 10.1021/acs.nanolett.5b00175.
46 A. Kushima, *et al.*, Liquid cell transmission electron microscopy observation of lithium metal growth and dissolution: root growth, dead lithium and lithium flotsams, *Nano*

Energy, 2017, **32**, 271–279, DOI: 10.1016/j.nanoen.2016.12.001.

47 C. Hou, *et al.*, Operando Observations of SEI Film Evolution by Mass-Sensitive Scanning Transmission Electron Microscopy, *Adv. Energy Mater.*, 2019, **9**(45), 1902675, DOI: 10.1002/aenm.201902675.

48 W. Ye, *et al.*, Stable Nano-Encapsulation of Lithium Through Seed-Free Selective Deposition for High-Performance Li Battery Anodes, *Adv. Energy Mater.*, 2020, **10**(7), 1902956, DOI: 10.1002/aenm.201902956.

49 C.-Y. Chen, T. Tsuda, Y. Oshima and S. Kuwabata, In Situ Monitoring of Lithium Metal Anodes and Their Solid Electrolyte Interphases by Transmission Electron Microscopy, *Small Struct.*, 2021, **2**(6), 2100018, DOI: 10.1002/sstr.202100018.

50 H. Sun, *et al.*, In Situ Visualization of Lithium Penetration through Solid Electrolyte and Dead Lithium Dynamics in Solid-State Lithium Metal Batteries, *ACS Nano*, 2021, **15**(12), 19070–19079, DOI: 10.1021/acsnano.1c04864.

51 C. Gong, *et al.*, Revealing the Role of Fluoride-Rich Battery Electrode Interphases by Operando Transmission Electron Microscopy, *Adv. Energy Mater.*, 2021, **11**(10), 2003118, DOI: 10.1002/aenm.202003118.

52 S. Lang, *et al.*, Multidimensional visualization of the dynamic evolution of Li metal via in situ/operando methods, *Proc. Natl. Acad. Sci. U. S. A.*, 2023, **120**(7), e2220419120, DOI: 10.1073/pnas.2220419120.

53 C.-F. Lin, A. C. Kozen, M. Noked, C. Liu and G. W. Rubloff, ALD Protection of Li-Metal Anode Surfaces – Quantifying and Preventing Chemical and Electrochemical Corrosion in Organic Solvent, *Adv. Mater. Interfaces*, 2016, **3**(21), 1600426, DOI: 10.1002/admi.201600426.

54 F. Lin, *et al.*, Synchrotron X-ray Analytical Techniques for Studying Materials Electrochemistry in Rechargeable Batteries, *Chem. Rev.*, 2017, **117**(21), 13123–13186, DOI: 10.1021/acs.chemrev.7b00007.

55 F. Tang, *et al.*, Synchrotron X-Ray Tomography for Rechargeable Battery Research: Fundamentals, Setups and Applications, *Small Methods*, 2021, **5**(9), 2100557, DOI: 10.1002/smtd.202100557.

56 J. Nelson Weker and M. F. Toney, Emerging In Situ and Operando Nanoscale X-Ray Imaging Techniques for Energy Storage Materials, *Adv. Funct. Mater.*, 2015, **25**(11), 1622–1637, DOI: 10.1002/adfm.201403409.

57 M. Wolfman, B. M. May and J. Cabana, Visualization of Electrochemical Reactions in Battery Materials with X-ray Microscopy and Mapping, *Chem. Mater.*, 2017, **29**(8), 3347–3362, DOI: 10.1021/acs.chemmater.6b05114.

58 L. Wang, J. Wang and P. Zuo, Probing Battery Electrochemistry with In Operando Synchrotron X-Ray Imaging Techniques, *Small Methods*, 2018, **2**(8), 1700293, DOI: 10.1002/smtd.201700293.

59 J.-H. Cheng, *et al.*, Visualization of Lithium Plating and Stripping via *in Operando* Transmission X-ray Microscopy, *J. Phys. Chem. C*, 2017, **121**(14), 7761–7766, DOI: 10.1021/acs.jpcc.7b01414.

60 J. H. Um and S.-H. Yu, Unraveling the Mechanisms of Lithium Metal Plating/Stripping via In Situ/Operando Analytical Techniques, *Adv. Energy Mater.*, 2021, **11**(27), 2003004, DOI: 10.1002/aenm.202003004.

61 S. Yang, *et al.*, *In situ* characterization of lithium-metal anodes, *J. Mater. Chem. A*, 2022, **10**(35), 17917–17947, DOI: 10.1039/D2TA04309B.

62 J. B. Cook, T. C. Lin, E. Detsi, J. N. Weker and S. H. Tolbert, Using X-ray Microscopy To Understand How Nanoporous Materials Can Be Used To Reduce the Large Volume Change in Alloy Anodes, *Nano Lett.*, 2017, **17**(2), 870–877, DOI: 10.1021/acs.nanolett.6b04181.

63 M. Olivares-Marín, A. Sorrentino, R.-C. Lee, E. Pereiro, N.-L. Wu and D. Tonti, Spatial Distributions of Discharged Products of Lithium–Oxygen Batteries Revealed by Synchrotron X-ray Transmission Microscopy, *Nano Lett.*, 2015, **15**(10), 6932–6938, DOI: 10.1021/acs.nanolett.5b02862.

64 B.-K. Cho, S.-Y. Jung, S.-J. Park, J.-H. Hyun and S.-H. Yu, *In Situ*/*Operando* Imaging Techniques for Next-Generation Battery Analysis, *ACS Energy Lett.*, 2024, **9**(8), 4068–4092, DOI: 10.1021/acsenergylett.4c01098.

65 Y. Wu and N. Liu, Visualizing Battery Reactions and Processes by Using *In Situ* and *In Operando* Microscopies, *Chem*, 2018, **4**(3), 438–465, DOI: 10.1016/j.chempr.2017.12.022.

66 J. Lim, *et al.*, Origin and hysteresis of lithium compositional spatiodynamics within battery primary particles, *Science*, 2016, **353**(6299), 566–571, DOI: 10.1126/science.aaf4914.

67 Y. Li, *et al.*, Current-induced transition from particle-by-particle to concurrent intercalation in phase-separating battery electrodes, *Nat. Mater*, 2014, **13**(12), 1149–1156, DOI: 10.1038/nmat4084.

68 M. Dorri, A. Kumar M. R. and K. Zaghib, In operando and in situ characterization tools for advanced rechargeable batteries: effects of electrode origin and electrolyte, *J. Power Sources*, 2025, **658**, 238188, DOI: 10.1016/j.jpowsour.2025.238188.

69 Y. Jeoun, *et al.*, Surface Roughness-Independent Homogeneous Lithium Plating in Synergetic Conditioned Electrolyte, *ACS Energy Lett.*, 2022, **7**(7), 2219–2227, DOI: 10.1021/acsenergylett.2c00974.

70 J. H. Um, S.-J. Kim, J.-H. Hyun, M. Kim, S.-H. Lee and S.-H. Yu, Real-Time Visualizing Nucleation and Growth of Electrodes for Post-Lithium-Ion Batteries, *Acc. Chem. Res.*, 2023, **56**(4), 440–451, DOI: 10.1021/acs.accounts.2c00652.

71 S.-H. Yu, X. Huang, J. D. Brock and H. D. Abruña, Regulating Key Variables and Visualizing Lithium Dendrite Growth: An *Operando* X-ray Study, *J. Am. Chem. Soc.*, 2019, **141**(21), 8441–8449, DOI: 10.1021/jacs.8b13297.

72 A. M. Tripathi, W.-N. Su and B. J. Hwang, *In situ* analytical techniques for battery interface analysis, *Chem. Soc. Rev.*, 2018, **47**(3), 736–851, DOI: 10.1039/C7CS00180K.

73 K. J. Harry, D. T. Hallinan, D. Y. Parkinson, A. A. MacDowell and N. P. Balsara, Detection of subsurface structures underneath dendrites formed on cycled lithium metal electrodes, *Nat. Mater*, 2014, **13**(1), 69–73, DOI: 10.1038/nmat3793.

74 S. E. Sandoval, *et al.*, Visualizing diverse lithium growth and stripping behaviors in anode-free solid-state batteries with operando X-ray tomography, *EES Batteries*, 2025, DOI: **10.1039/D5EB00111K**.

75 J. H. Um, S.-J. Kim, J.-H. Hyun, M. Kim, S.-H. Lee and S.-H. Yu, Real-Time Visualizing Nucleation and Growth of Electrodes for Post-Lithium-Ion Batteries, *Acc. Chem. Res.*, 2023, **56**(4), 440–451, DOI: **10.1021/acs.accounts.2c00652**.